Microseismicity of the Mid-Atlantic Ridge at 7°S–8°15′S and at the Logatchev Massif oceanic core complex at 14°40′N–14°50′N

Ingo Grevemeyer
GEOMAR Helmholtz Centre of Marine Research, Kiel DE-24148, Germany (igrevemeyer@geomar.de)

Timothy J. Reston
School of Earth and Environmental Sciences, University of Birmingham, Birmingham, UK

Stefan Moeller
GEOMAR Helmholtz Centre of Marine Research, Kiel DE-24148, Germany

[1] Lithospheric formation at slow spreading rates is heterogeneous with multiple modalities, favoring symmetric spreading where magmatism dominates or core complex and inside corner high formation where tectonics dominate. We report microseismicity from three deployments of seismic networks at the Mid-Atlantic Ridge (MAR). Two networks surveyed the MAR near 7°S in the vicinity of the Ascension transform fault. Three inside corner high settings were investigated. However, they remained seismically largely inactive and major seismic activity occurred along the center of the median valley. In contrast, at the Logatchev Massif core complex at 14°45′N seismicity was sparse within the center of the median valley but concentrated along the eastern rift mountains just west of the serpentine hosted Logatchev hydrothermal vent field. To the north and south of the massif, however, seismic activity occurred along the ridge axis, emphasizing the asymmetry of seismicity at the Logatchev segment. Focal mechanisms indicated a large number of reverse faulting events occurring in the vicinity of the vent field at 3–5 km depth, which we interpret to reflect volume expansion accompanying serpentinization. At shallower depth of 2–4 km, some earthquakes in the vicinity of the vent field showed normal faulting behavior, suggesting that normal faults facilitates hydrothermal circulation feeding the vent field. Further, a second set of cross-cutting faults occurred, indicating that the surface location of the field is controlled by local fault systems.

1. Introduction

[2] A key tenet of plate tectonics is that magnetic spreading anomalies observed over mid-ocean ridges and the ocean basins arise because seafloor spreading records the episodic polarity reversals of the geomagnetic field [*Vine and Matthews*, 1963]. Thus, seafloor magnetized at the ridge crest is rifted apart by seafloor spreading, transferring crust emplaced within the median valley to either side of the spreading axis, causing a roughly identical set of anomalies on both ridge flanks.

[3] However, at slow-spreading ridges were magma supply is variable both in time and space spreading is accommodated by different modes. The first mode is dominated by magmatic processes with subsidiary high-angle normal faulting and the formation of abyssal hills on both flanks, resulting into the well-known symmetrical accretion of lithosphere [e.g., *Escartín et al.*, 2008] as envisioned in early models of seafloor spreading. The second mode is related to the formation of detachment faults [*Cann et al.*, 1997; *Smith et al.*, 2006; *Escartín et al.*, 2008; *Reston and Ranero*, 2011]. The formation of oceanic detachment faults and associated oceanic core complexes (OCC) is well established from inactive, corrugated fault planes exposed on sea floor formed along slow and ultra-slow spreading centers and can accommodate extension for up to 1–3 Myr [e.g., *Tucholke et al.*, 1998; *Baines et al.*, 2008]. This complex accretion process may give rise to poorly developed and sometimes discontinuous spreading anomalies when compared to fast-spreading ridges [e.g., *Vogt*, 1986].

[4] Detailed magnetic surveys of the Mid-Atlantic Ridge (MAR) [e.g., *Tivey and Tucholke*, 1998; *Fujiwara et al.*, 2003] suggested, however, that accretion is still confined to the median valley. Local seismicity surveys generally support this view, indicating that seismicity is generally concentrated along the ridge axis [*Kong et al.*, 1992; *Wolfe et al.*, 1995; *Barclay et al.*, 2001] and hence roughly mimic the neovolcanic zone, though some activity occurs at the flanking rift mountains [*Toomey et al.*, 1988; *Kong et al.*, 1992; *Tilmann et al.*, 2004; *Collins et al.*, 2012]. In addition, some of the local networks suggested that near-oceanic core complexes we may expect tectonic activity at and below OCCs [*Wolfe et al.*, 1995; *Barclay et al.*, 2001; *Collins et al.*, 2012]. Monitoring the regional seismicity of the Mid-Atlantic Ridge using autonomous hydrophone arrays [*Smith et al.*, 2003; *Simao et al.*, 2010] indicated that there is an excellent correlation between the mode of accretion and the seismicity along the ridge axis [*Escartín et al.*, 2008; *Simao et al.*, 2010]. The hydroacoustic catalogue is complementary to global catalogues and showed that detachment dominated, asymmetrical ridge sections host >50% more hydroacoustic events than symmetrical segments. The concentration of seismicity at segments shown to have active detachment faults, such as the Logachev massif south of the Fifteen-Twenty transform fault, is hence suggested to be a general feature [*Escartín et al.*, 2008].

[5] Two studies delineating the seismicity of core complexes are available; one in the vicinity of the TAG hydrothermal vent field near 26°8'N [*deMartin et al.*, 2007] and the second survey at the Atlantis Massif [*Collins et al.*, 2012]. At the TAG field, microseismicity indicates that the detachment fault is indeed seismically very active, and suggests that the fault is rooted in the neovolcanic zone near the center of the median valley. The survey at the Atlantis Massif supported the observation that seismicity occurred predominantly in the median valley, however, some minor activity was located below the core complex. Neither of the experiments revealed profound seismicity emerging at the core complex itself as detected in hydoacoustical catalogues [*Smith et al.*, 2003; *Escartín et al.*, 2008; *Simao et al.*, 2010].

[6] Hydroacoustic detection of earthquakes is based on T waves that travel over large distances through the Sound Fixing and Ranging (SOFAR) channel and hence represents the point where T wave energy enters the sound channel once the energy is radiated into the water column from seismic body waves reaching the seafloor. The complexity of conversion of seismic energy into T wave energy and the rough topography of slow-spreading ridges make it difficult to directly estimate the earthquake source location [*Williams et al.*, 2006], although some activity observed by hydrophone arrays may suggest that seismic activity is indeed shifted away from the center of the median valley [*Simao et al.*, 2010], occurring at the flanking rift mountains. However, much tighter error bounds for event detection are needed to better understand the relationship between lithospheric formation, tectonism, and earthquake occurrence.

[7] Here, we report results from two microseismicity surveys at the Mid-Atlantic Ridge in the vicinity of the Ascension transform fault and a third deployment to the south of the 15°20'N transform in the vicinity of the Logatchev hydrothermal vent field. All three survey areas included oceanic core

complexes or inside corner highs identified in bathymetric data.

2. Tectonic Setting

2.1. Area-1: The Mid-Atlantic Ridge at 7°S–8°15′S

[8] The Ascension fracture zone at 7°S to the northeast of Ascension Island consists of a double transform with an intervening 20 km long spreading segment (Figure 1); we call this segment the Ascension intratransform segment. The short intervening spreading segment is characterized by a deep valley of >4500 m. The off-axis trace of the spreading segment further east was mapped by Seabeam swath bathymetry [*Brozena and White*, 1990] (N. Cherkis, unpublished data, 1985) providing corrugated surfaces, indicating unroofing of lower crustal and upper mantle rocks at an inside corner high setting. Dredging during R/V *Meteor* cruise M41 confirmed this idea by providing serpentinized peridotites and gabbroic rocks (C. Devey, personal communication, 2004). Immediately to the south of the Ascension fracture zone in segment A1 [*Bruguier et al.*, 2003], the median valley changes from a trough-like feature to an axial high south of 8° 30′S. At the intersection between segment A1 and the transform fault, a blocky inside corner massif is present. Dredge samples provided gabbroic rocks from the flank of the inside corner high that faces the median valley (C. Devey, personal communication, 2004). Dredging further south along the median valley provided exclusively basaltic samples.

2.2. Area-2: The Mid-Atlantic Ridge to the South of the 15°20′N Transform Fault

[9] The Logatchev hydrothermal vent site is located roughly 60 km to the south of the 15°20′N transform fault at 3000 m water depth on the eastern rift shoulder (Figures 2 and 3). The site is roughly 8 km off axis and 1000 m shallower then the median valley, occurring in the segment S2 named by *Fujiwara et al.* [2003]. Studies of vent fluids [*Bogdanov et al.*, 1997] and alteration of rocks from the Logatchev massif [*Augustin et al.*, 2012; *Petersen et al.*, 2009] indicated that the Logatchev vents are located in a serpentinite hosted setting. Bathymetric mapping and dredging supported the idea that the hydrothermal activity is related to core complex formation [*Escartin and Cannat*, 1999; *Fujiwara et al.*, 2003]. Site 1270 drilled during the Integrated Ocean Drilling Program (IODP) leg 209 corroborated these facts by recovering gabbros and mantle rocks from the massif [*Shipboard Scientific Party*, 2004].

3. Seismological Data

3.1. Area-1: Ascension Deployments

[10] Two of the deployments reported here were made in the vicinity of the Ascension transform fault. In the Ascension intratransform segment, deployment 1 had 11 ocean bottom hydrophones (OBH) and one three-component 4.5 Hz seismometer (OBS). Instruments were deployed over a short time period of 13 days in October 2004. Station separation was <5 km (Figure 1b). Unfortunately, two stations near the northwestern rift valley bounding fault failed to record any data.

[11] The deployment 2 was to the south of the Ascension transform fault and was primarily deployed for a wide-angle survey and then left on the seafloor to detect local seismicity. In total, 18 OBH and OBS were deployed over a time period of 6 weeks in October and November 2004. The array consisted of two profiles running roughly along the western and eastern bounding faults of the median valley. The network suffered from three stations that failed to record any data and also the northwestern-most station failed after a few days. Further, instrument spacing was in the order of 10 km and hence station separation was about twice as large as chosen for deployment 1 (Figure 1c).

3.2. Area-2: Logatchev Deployment

[12] In the vicinity of the Logatchev hydrothermal vent field we had two deployments that overlapped in time (Figures 2 and 3). The first deployment was a small array of four broadband OBS that were operated between 16 December 2007 and 2 February 2009. Each OBS operated a three-component Guralp CMG-40T seismometer and a HighTech HTI-04-PCA/ULF hydrophone. Unfortunately, one of the OBS was lost. The second deployment consisted of 12 OBS deployed between 16 and 21 January 2009 and instruments were recovered on 25 and 26 March 2009. The second deployment operated hydrophones and three-component short-period seismometers with a natural frequency of 4.5 Hz. One OBS failed to record any data. Here, we will report results from all OBS available at the seabed after 16 January 2009. Data quality is excellent, providing clear *P*- and *S*-onsets on most stations (Figure 4).
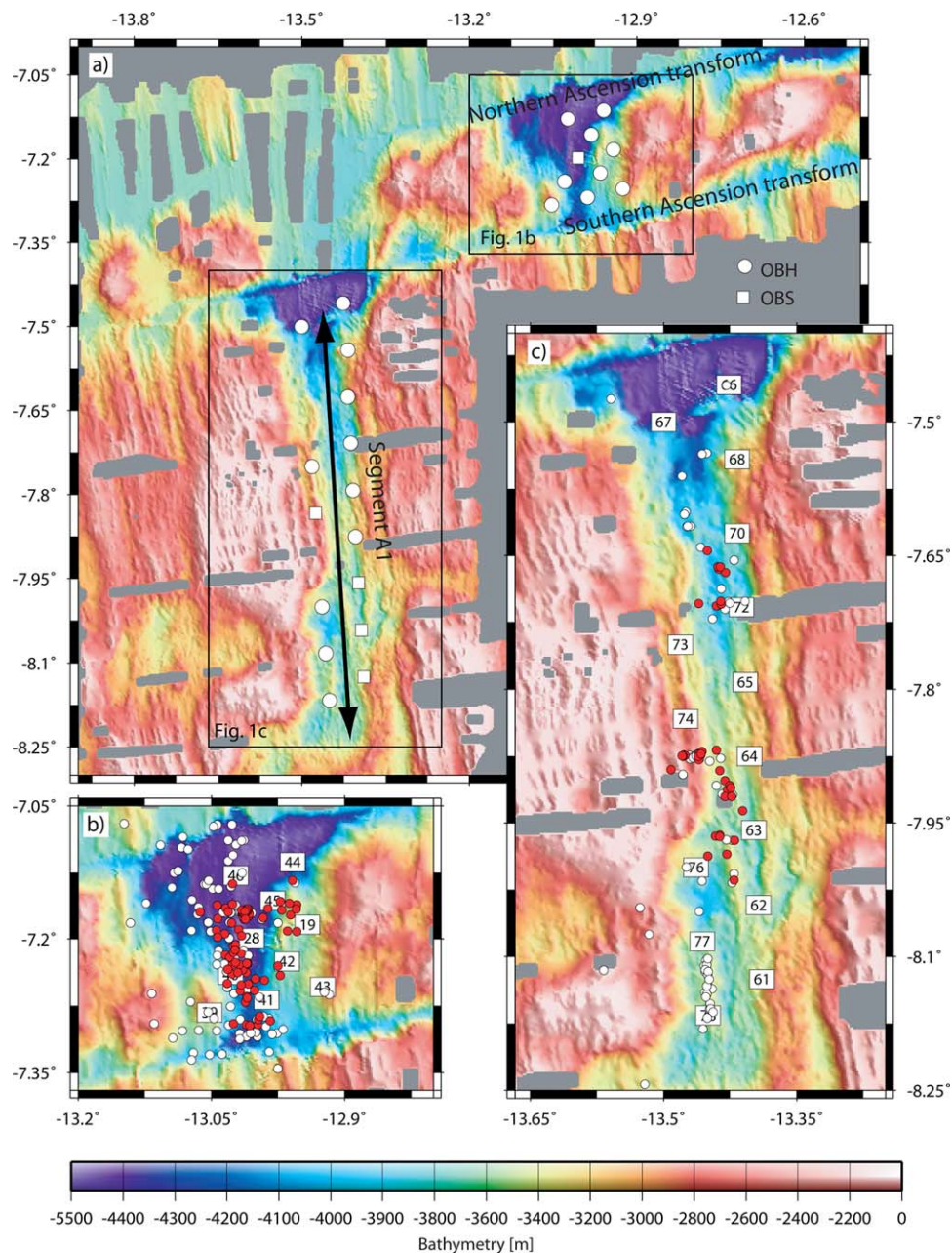
Figure 1. Deployments 1 and 2: (a) Morphology at the Mid-Atlantic Ridge in the vicinity of the Ascension double transform fault [*Brozena and White*, 1990; *Minshull et al.*, 2003]; (b) Microseismicity deployment 1 at the 20 km wide segment sandwiched between the double transform fault, OBS/H are numbered squares; earthquake epicenters are marked by dots; red dots are well-located events; (c) Microseismicity deployment 2 to the south of the Ascension transform fault.

4. Methods

4.1. Event Detection and Localization

[13] To detect automatically seismic events in the continuous records a short-term-average versus a long-term-average (STA/LTA) trigger algorithm was applied. We used a STA window of 0.5 s and a LTA window of 60 s. The trigger ratio was 4.0 and the detrigger ratio was 2.5. The trigger parameters were applied to unfiltered vertical component data. For the deployments in the vicinity of the Ascension transform, where only a few OBS were available, we used instead good quality hydrophone channels. We consider a trigger to be an earthquake when it was detected on more than five
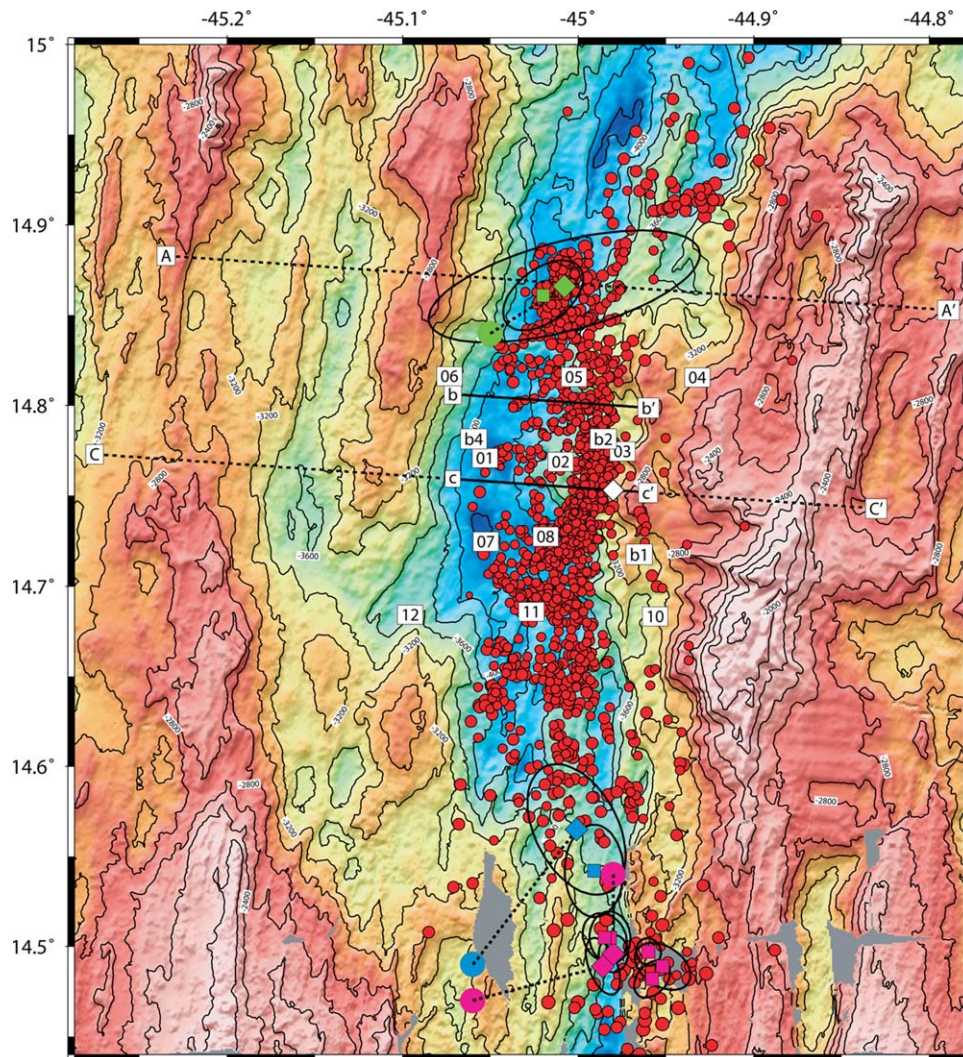
Figure 2. Deployment 3 to the south of the 15°20′N transform fault at the Logatchev Massif. Logatchev high-temperature vent field is marked by white diamond. Two deployments were conducted in the area that overlapped in time. The first deployment had three broadband OBS (labeled b1, b2, and b4), the second 11 short-period OBS (labeled 01 to 12). Large colored circles are globally recorded events plotted at the USGS epicenter. Diamonds with the same color and 95% error ellipses are the relocated epicenters based on the local network. Smaller squares with the same color and error ellipse are aftershocks. Small red circles are all local earthquakes that were sampled with our network. Bathymetry was collected during cruise MSM10/3 of the R/V *Maria S. Merian*. Labeled transects are shown in Figures 5 and 11. Same color scale as in Figure 1.

stations for deployments 1 and 2. For the Logatchev deployment, a trigger had to occur on at least eight OBS. With these trigger parameters, visual inspection of the data suggests that we obtained generally less than ~10% false triggers and missed events that were recorded only on a few stations, while all major events were included. For event detection, we extracted a 3 min long time window from the continuous data, starting 20 s prior to trigger time. Events were registered into a SEISAN database [*Havskov and Ottemöller*, 2000] and *P* wave and *S* wave arrival times were hand-picked.

[14] Earthquakes were located with the program HYPOCENTER, which employs an iterative solution to the nonlinear localization problem [*Lienert et al.*, 1986; *Lienert and Havskov*, 1995]. To compensate effects caused by differences in elevation and shallow velocity structure station corrections were introduced. Travel times were calculated using a 1-D velocity model. Unfortunately, no seismic refraction work was conducted in the areas. We therefore based our model on constraints from work previously conducted along slow-spreading ridges [e.g., *Canales et al.*, 2000; *Minshull et al.*, 2006; *Dannowski et al.*, 2010, 2011]. However,
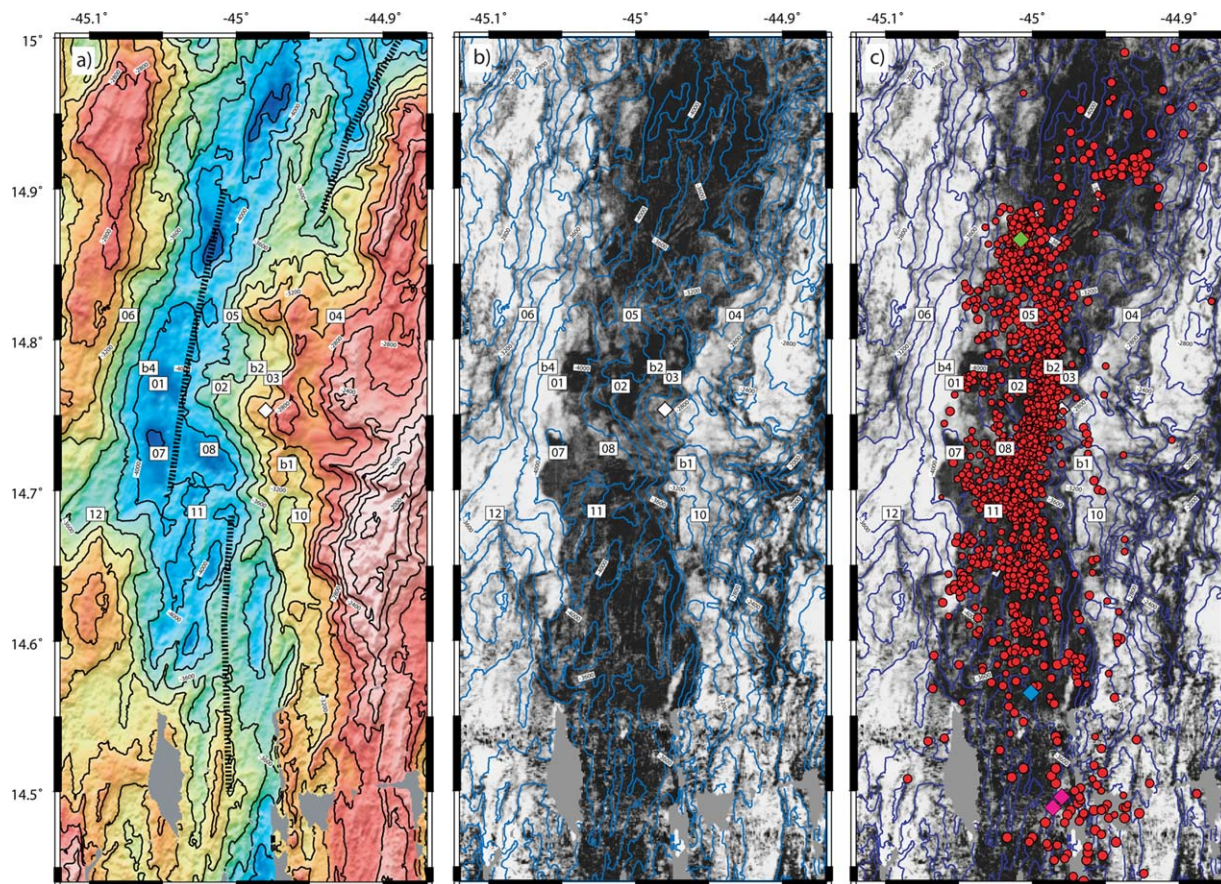
Figure 3. Deployment 3—Logatchev Massif: (a) bathymetry and network location. Broken lines mark the location of zero-age curst based on bathymetry and magnetics (modified from *Escartin and Cannat* [1999], *Fujiwara et al.* [2003], and *Escartín et al.* [2008]); (b) backscatter intensity derived from EM120 swath mapping. High backscatter (dark black) indicates younger seabed, lower backscatter (lighter gray) older sedimented seabed; (c) same as Figure 3b but with earthquake locations. Labels and symbols as in Figure 2.

overall the velocity structure of zero-aged crust is reasonably similar, with a high-gradient upper crustal velocity structure and a low gradient lower crust. Velocities in the upper crust (layer 2) increase rapidly from 2.5–3 km/s to 6.2–6.7 km/s at 1.5–2 km depth, while velocity in the lower crust (layer 3) remains with 6.8–7.0 km/s almost constant. Major changes, however, may occur in the thickness of the lower crust. We therefore surveyed a number of models with crustal thickness varying from 3 to 7 km. Overall, changes in crustal thickness had only a small effect on both epicentral location and depth, indicating a trade-off between origin time and crustal thickness. Thus, using a thicker crust resulted in an earlier origin time, while a thinner crust caused later origin times. The depth of the earthquakes, however, changed very little and most earthquakes occurred at 3–6 km below seafloor, a feature that has been previously observed for most microearthquake surveys at the

Mid-Atlantic Ridge [e.g., *Toomey et al.*, 1988; *Kong et al.*, 1992; *Wolfe et al.*, 1995; *Barclay et al.*, 2001]. Interpretation of the data, however, would be different; thus, for the case of a thinner crust earthquakes would occur predominantly in the mantle and in thicker crust events would tend to occur in the crust. The crustal thickness of the preferred models was hence constrained by gravity data, indicating 6 km of crust for the segments in the vicinity of the Ascension fracture zone [*Minshull et al.*, 2003] and 5 km for the crust in the vicinity of the Logatchev vent field [*Fujiwara et al.*, 2003]. For interpretation, we used the gravity-based estimates of crustal thickness.

[15] A shortcoming of using a 1-D velocity model is, of course, that 2-D and 3-D effects are not accounted for. Such structural variability has been reported for a number of core complexes [e.g., *deMartin et al.*, 2007; *Dannowski et al.*, 2010]. However, most detected events occurred in the
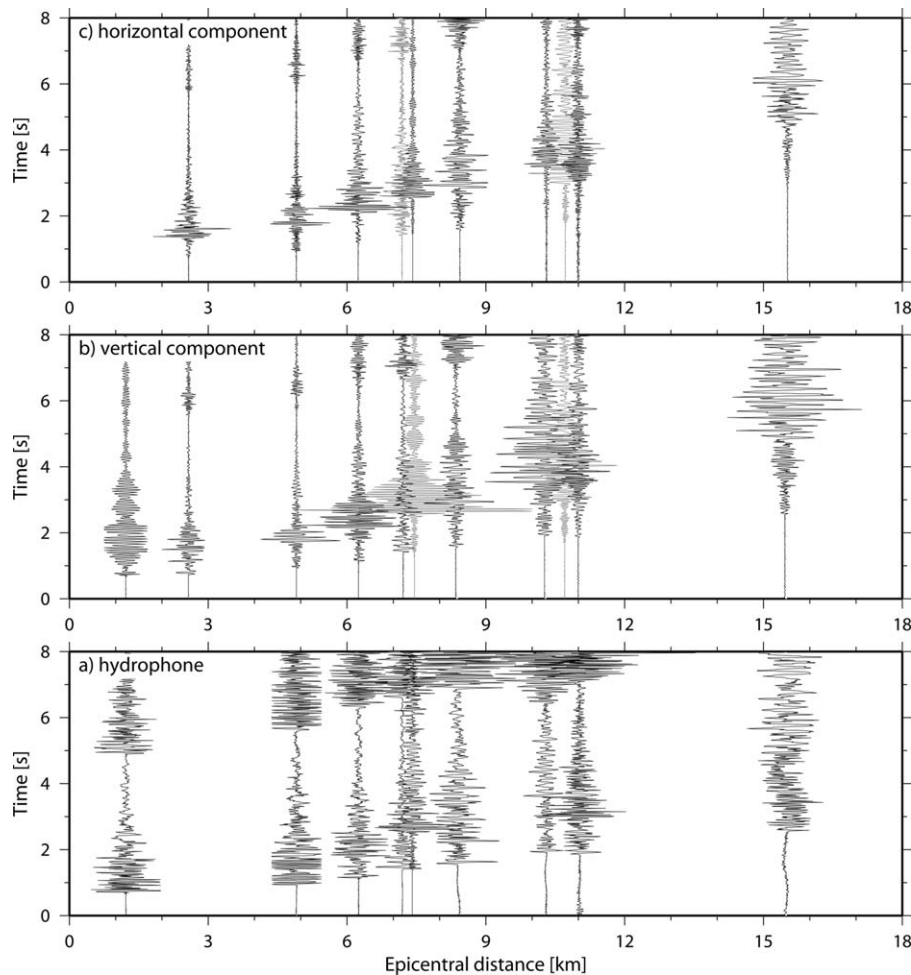
Figure 4. Deployment 3—Logatchev Massif: example of a $M_L = 3.6$ event recorded on 3 February 2009 at the 11 short-period seismometers.

median valley and below the flanking bounding fault. Thus, a 1-D model provides a reasonable approximation.

[16] The S wave velocity structure of oceanic crust is much less well constrained than the P wave velocity. We tested a number of different Vp/Vs ratios ranging from 1.75 to 2.0. For events located within the network, most changes were much smaller than the 95% error estimates. For earthquakes outside of the network, however, smaller Vp/Vs ratios shifted the events farther and larger rations closer to the network. Changes, however, were generally smaller than 5 km.

[17] To further constrain the Vp/Vs ratio, we reviewed previous surveys on the structure of crust formed at the Mid-Atlantic Ridge. *Dannowski et al.* [2011] provided the only seismic refraction and wide-angle survey that observed converted S waves in an active source seismic experiment at

the Mid-Atlantic Ridge and report Vp/Vs ratios in the order of 1.7–1.9. Geophysical measurements during Ocean Drilling Program (ODP) leg 102 at Deep Sea Drilling Project (DSDP) hole 418A yielded in the upper basaltic crust Vp/Vs ratios of 1.89 and 1.84 from downhole logging and laboratory measurements at 0.1 kbar, respectively [*Salisbury et al.*, 1988]. Gabbros were drilled at the Atlantis Bank, South West Indian Ridge, and in the MARK area at the Mid-Atlantic Ridge. Laboratory studies at confining pressure yielded for gabbros from the Atlantic Bank in the hole 735B Vp/Vs ratios of 1.75 to 1.83 [*Iturrino et al.*, 1991], averaging 1.78. For the MARK area, observed Vp/Vs ratios range from 1.76 to 1.87, averaging 1.83 [*Miller and Christensen*, 1997]. Drilling in the MARK area also provided serpentinized mantle with Vp/Vs ratios ranging from 1.8 to 2.2 [*Miller and Christensen*, 1997]. Based on these estimates, we used an average Vp/Vs ratio of 1.84 for

locating events outside of the network. For events within the network, we used Wadati diagrams (S-P time versus P time) and calculated an average Vp/Vs ratio [*Havskov and Ottemöller*, 2000]. To constrain the Vp/Vs ratio, we used 402 earthquakes with at least eight *P* wave and *S* wave pairs, an RMS event location misfit of 0.1 or better, and a correlation coefficient of the fit of S-P time versus P time of >0.9. The resulting Vp/Vs ratio was 1.79.

4.2. Location Uncertainties and Errors

[18] The uncertainty of a hypocenter is related to a number of features, including picking uncertainty, number of stations, number of *P* and *S* wave onsets, and station spacing. For most onsets, picking uncertainty was in the order of 10–40 ms for P onsets and 20–60 ms for S onsets. We consider an event being well located when the horizontal error $ERH < 20$ km and the error in depth $ERZ < 10$ km. In practice, however, errors for the well-located events were much smaller. The average error for event location depended on the network layout and performance and ranged for ERH from 7 to 2 km and for erz from 6 to 3 km. Table 1 indicates the characteristic values of all three networks.

4.3. Magnitudes

[19] We defined magnitudes based on the classical approach of *Richter* [1935] and used local magnitude or M_L. Thus, the magnitude is proportional to the maximum amplitude A of the displacement of a Wood-Anderson seismometer for frequencies $f > 1.25$ Hz; thus, $M_L \sim \log_{10}(A)$. In order to use the M_L scale with other instruments than the Wood-Anderson seismometer, the common practice is to generate a displacement trace in the frequency band 1.25–20 Hz and measure the maximum amplitude.

[20] *Kanamori* [1983] showed that for magnitudes of 4–6 M_L and M_W are in good agreement. How-

ever, for smaller magnitudes ($M_L < 2$–4), this is generally not the case [e.g., *Havskov and Ottemöller*, 2010]. This observation has been explained by the response of the Wood Anderson instrument. For small events, which have high frequencies, the signal measured is pure displacement and it is therefore expected to be linearly proportional to M_0. Thus, M_L will be linearly proportional to $\log_{10}(M_0)$ and $M_L \sim \log_{10}(M_0) \sim 1.5 M_W$ or $M_W \sim 0.67 M_L$. For larger events with significant energy below 1.25 Hz, the maximum amplitude will be more proportional to velocity and therefore closer to the response of the traditional velocity sensors.

4.4. Source Parameters

[21] First motion *P* wave polarities are commonly used to determine double-couple focal mechanisms for marine microearthquake studies. Fault plane solutions were derived using the HASH and FOCMEC algorithms [*Hardebeck and Shearer*, 2002; *Snoke et al.*, 1984]. We report only those mechanisms where both approaches provided reasonable similar solutions.

5. Results

5.1. Rate of Seismicity and Detection Threshold

[22] Over the 13 day recording period, 206 earthquakes were obtained during deployment 1 in the Ascension intratransform segment (Figure 1b), averaging 16 earthquakes per day in a network of 10 recording stations of 20 km by 15 km in size and stations spaced at ~5 km intervals. To the south of the Ascension transform, the seismic activity recorded over the 24 day experiment was much lower; 121 earthquakes were obtained during deployment 2 (Figure 1c), indicating 5 earthquakes per day in a network of 15 recording stations covering an area of 80 km by 10 km and a spacing of OBH of ~10 km. The deployment in

Table 1. Performance and Statistical Errors for All Three Deployments[a]

Network	Number of Earthquakes (Recording Time)	Magnitude Range	Number of Earthquakes[b] (ERH < 20 km, ERZ < 10 km)	ERH (km) for Events in Column 4	ERZ (km) for Events in Column 4	Mean Depth (km) for Events in Column 4	Average RMS (s) Misfit for Events in Column 4
Ascension network 1	206 (13 days)	−0.2–1.6	95	5.49	4.5	5.05	0.025
Ascension network 2	121 (24 days)	1.2–3	35	6.99	5.8	3.2	0.036
Logatchev	1618 (67 days)	0.4–4.4	699	2.34	2.96	4.29	0.078

[a]erh, horizontal error; ehz, vertical error.
[b]Observed at five or more stations for deployment 1 and 2 and at seven or more stations for Logatchev deployment.

the vicinity of the Logatchev Massif provided with 1618 earthquakes, the largest number of events. Thus, for the 67 day period we could locate on average 24 earthquakes per day on 11–14 OBS deployed in a network of 18 km by 18 km in size. For the Logatchev deployment, OBS spacing was variable, ranging from 5 to 10 km. Individual OBS, however, provided much higher seismicity rates based on the STA/LTA triggers and visual inspection of stations with high rates. Thus, some OBS provided 100 or more triggers, suggesting that seismicity varies profoundly on a small spatial scale. Such events will have generally magnitudes <0.5. Similar features were reported from previous deployments at the Mid-Atlantic Ridge [e.g., *Kong et al.*, 1992; *Wolfe et al.*, 1995].

[23] The detection threshold was quite variable between the different deployments, depending on stations' spacing and local tectonics. For the two deployments in the vicinity of the Ascension transform fault, we used the spectra to assess magnitudes from hydrophone recordings. Fortunately, for the Logatchev deployment, we had short-period and broadband seismometers with known sensor responses and hence used local magnitude M_L. Deployment 2 detected earthquakes as small as $M \sim$ 1.2–1.5. The largest events were in the order of $M \sim$ 3. Deployment 1 recorded much smaller earthquakes. The largest was $M \sim 1.6$ and the majority of seismicity had much smaller magnitude. We therefore had difficulties identifying corner frequencies in the 100 Hz data. One station operated a seismometer and magnitudes were in the order of $M_L \sim -0.2$ to 1.5. For the deployment to the south of the 15°20' transform at the Logatchev Massif, the smallest magnitudes were in the order of $M_L \sim 0.4$ to 0.6. However, as discussed later, the magnitude of completeness was with $M_L = 1.3$ much larger.

[24] It is interesting to note that the broadband OBS (dynamic range 140 dB), with respect to the short-period OBS (dynamic range 100 dB), performed less successfully in recording clear *P* onsets of earthquakes with magnitudes of smaller ~ 1.5. This feature might be related to the ambient noise that increases at lower frequencies in the ocean. Thus, for small events the ambient ocean noise dominated the wavefield sampled with the CMG-40T and the dynamic range of the recording unit was too small for obtaining high-quality recordings of weak *P* onsets. However, *S* wave energy was generally detected. Therefore, the restriction of the bandwidth for the short-period sensors nurtured sampling small magnitude events.

5.2. Distribution of Microseismicity

[25] The two deployments in area-1 provided reasonable similar pattern. Deployment 1 in the Ascension intratransform segment indicated that seismicity was primarily focused along the center of the median valley and hence at the deepest portion of the rift (Figure 1b). At the northern end of the segment, however, a well-defined inside corner high occurred. Some of the well-located microearthquake clustered at the inside corner high next to the active transform fault.

[26] To the south of the Ascension transform fault, most earthquakes occurred along the center of the valley. Perhaps suffering from instrument failure, we did not detect any seismicity at the inside corner high. Except for a single cluster of activity to the west of OBS64 near 7.875°S, seismicity to the south of 7.8°S coincided with the axial volcanic ridge (Figure 1c).

[27] In area-2 to the south of the 15°20'N, transform fault boundary seismicity indicates a quite different distribution (Figures 2, 3, and 5). To the north and south of the Logatchev Massif core complex seismicity showed the expected pattern and clustered along the center of the median valley. At the core complex between 14.7°N and 14.8°N, however, seismicity was clearly shifted away from the center of median valley and deepest portion of the rift valley and occurred westward of the Logatchev hydrothermal vent field at the walls of the inner valley.

[28] Side-scan sonar data can be used to assess recent magmatic activity at mid-ocean ridges [e.g., *Mitchell*, 1991] with high reflectivity regions representing seafloor that has experienced magmatism and low backscatter regions representing older seafloor covered with sediment. Backscatter images from swath-mapping bathymetric data can be used as first-order approximation of the backscatter intensity of the seabed. For the Logatchev area, backscatter data from the Kongsberg EM120 swath-mapping system operated during the cruise MSM10/3 of the R/V *Maria S. Merian* were available. High backscatter occurred within the median valley inward of the bounding faults (Figure 3). Basically, all earthquakes recorded with our network occurred within the area of high backscatter. Thus, major seismicity occurred within ±8 km of the ridge axis and hence within an area of magmatic activity in the recent past. Some minor activity, however, occurred 2–3 km to the east of the Logatchev hydrothermal field at a distance of ∼12 km off the ridge axis.
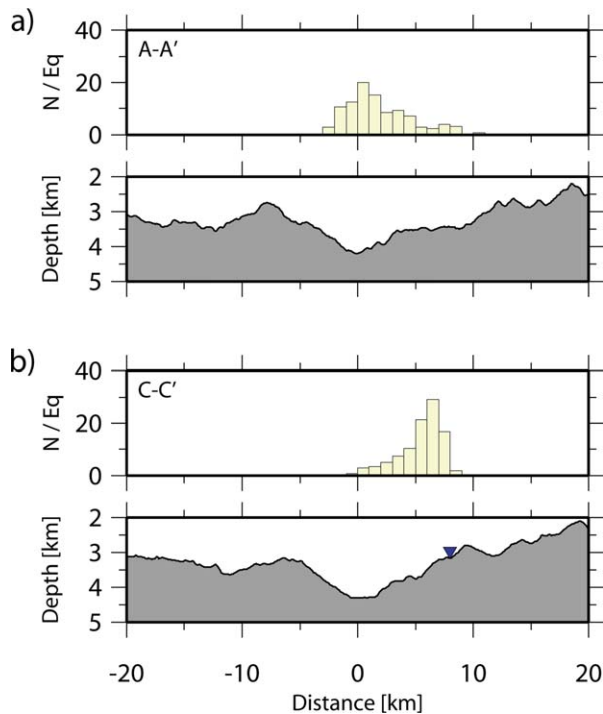
Figure 5. Deployment 3—Logatchev Massif: bathymetry and histograms of seismicity along the transects (a) A-A' (see Figure 2 for location) and (b) C-C'. Zero marks the location of the ridge axis. Events ±5 km off of the profiles were projected. Blue inverted triangle marks the location of the high-temperature Logatchev vent field. Note that seismicity clusters at the ridge axis along transect A-A' and occurs off axis along C-C'.

5.3. Distribution of Large Teleseismic Earthquakes

[29] During the time of operation of the network in the vicinity of the Logatchev Massif, we observed four earthquakes that were also detected by global seismic stations and reported by the International Seismological Centre (ISC) and the US Geological Survey (USGS). Even though the events did not occur within the network, they ruptured the rift valley within 10–20 km off the network. At such small offsets, the network provided a good longitudinal coverage so that the location within the median valley could be well constrained. In north-south direction, as discussed above while surveying V_p/V_s ratios, we may bias the location by approximately 5 km. The first two earthquakes, which occurred on 30 December 2008 at 14:57 and on 16 January 2009 at 22:14, respectively, were just recorded at the three broadband OBS. The 16 January earthquake was a $Mw = 5.4$ normal faulting event reported in the global centroid moment tensor (gCMT) catalogue. Two additional earthquakes were detected on 24 March 2009 at

11:56 and 12:34 and were recorded at 11 OBS just a day before recovering the network. To reduce the unknown parameters, we fixed the depth to 6 km for events occurring outside of the network. To further constrain the locations of the mainshocks, we identified a number of aftershocks following the mainshock within a few hours. All aftershocks occurred near the mainshock (Figures 2 and 3) and hence support location estimates. The largest deviation from the epicenter reported in the USGS PDE catalog and our estimates occurred for the $Mw = 5.4$ earthquake occurring on 16 January; it was shifted by 11 km to the northwest. The other earthquakes generally showed a similar shift in northeast direction, but the deviation was generally in the order of 5–7 km (Figure 2). Except for the 30 December earthquake, the USGS reported events occurred outside of the 95% confidence error ellipsoid.

[30] The 30 December 2008 earthquake occurred just 10 km to the north of the northernmost seismometer. After deployment of the second network in mid-January, we recorded a wealth of seismic activity from the epicentral region of the mainshock (Figures 2 and 3) supporting an area of intense seismic activity. The other three globally detected events occurred to the south of the network, roughly 15–20 km from the northernmost OBS. At this distance, we were only able to detect the largest aftershocks of magnitudes $M_L > 2$. Interestingly, all four earthquakes occurred in the deepest portion of the median valley.

5.4. Frequency-Size Distribution of Earthquakes

[31] Previous deployments at the MAR indicated that the frequency-size distribution of earthquakes provided information on the mode of spreading and can be used to discriminate between settings dominated by amagmatic extension and more recent volcanic activity [e.g., *Kong et al.*, 1992]. Only the network in area-2, and hence in the vicinity of the Logatchev Massif core complex, provided the required number of earthquakes to provide robust statistical estimates. With 10–30 events located per day (Figure 6), the network provided in the order of 1400 high-quality magnitude estimates. Most of the earthquakes detected by the Logatchev network had magnitudes of $M_L < 2$ (Figure 7). With distance from the network, the number of $M_L < 2$ clearly decreases, indicating that such small events are rarely observed 10–15 km away from the edges of the network. The number of events with $M_L \sim 2$–3 is larger at the edges of the

network. Interestingly, the smaller number of $M_L \sim$ 2–3 in the vicinity of the massif was inverse to the increase of $M_L < 2$ events. The network provided a detection threshold or magnitude of completeness of $M_L = 1.3$ and a b value of 0.9 for the seismicity at the Logatchev Massif and a b value of 1.2 for the median valley centered seismicity to the northwest of the massif (Figure 8), indicating along-axis changes of processes governing seismicity.

5.5. Focal Mechanisms

[32] We report a number of well-constrained focal mechanisms using first motion polarities. The most interesting feature is the large diversity of source parameters, including some well-resolved thrust faulting events, like the $M_L = 3.6$ earthquake of 3 February 2007 (Figures 4 and 9).

[33] In the beginning of the deployment in January 2009 we observed 10 events per day and normal faulting dominated (Figures 6 and 10a). However, at Julian day 25 the activity increased to ∼20 events per day and a small number of reverse faulting events was observed. In the second week of February pattern changed and reverse faulting dominated (Figure 10b). In March, between Julian days 65 and 70, both the number of reverse faulting earthquakes and the total number of event decreased (Figures 6 and 10c).
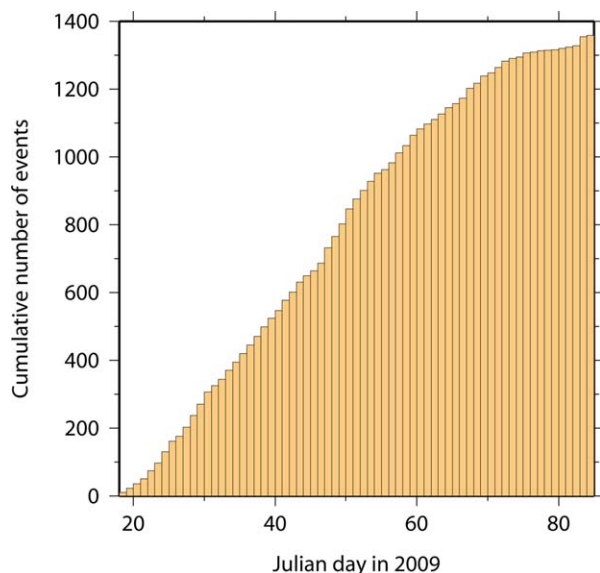

Figure 6. Deployment 3—Logatchev Massif: cumulative number of earthquakes detected by the network in the vicinity of the Logatchev Massif. Note, activity was reasonably constant at ∼10 to ∼20 events per day during most of the time. At Julian day 70, activity dropped significantly.

5.6. Depth Distribution of Microearthquakes

[34] At the Ascension intratransform segment earthquakes occurred at 4–6 km below seafloor, with the majority of events occurring at 4.5–5.5 km depth. The averaging depth of the 95 well-located events was 5.05 km (Table 1). Based on mantle bouguer anomalies (MBA), *Minshull et al.* [2003] found a crustal thickness of 6 km for the area to the south of the Ascension fracture zone. For the short segment itself crustal thickness might be lower. Considering a crustal thickness of 5 km earthquakes would occur in the lower crust and upper mantle. The majority of events would hence cluster at the crust/mantle boundary.

[35] The segment to the south of the Ascension transform has a crustal thickness of approximately 6 km [*Minshull et al.*, 2003]. Here, only 35 earthquakes were located well enough to provide reasonable good depth constraints. Most earthquakes are much shallower than at the segment to the north. Events occurred at 2–4 km depth below seafloor and hence within the crust.

[36] At the Logatchev Massif gravity data constrained a crustal thickness in the order of 5 km [*Fujiwara et al.*, 2003]. The 699 well-located earthquakes occurring within the network occurred at a depth of ∼1 to ∼6 km, with the majority of events occurring at 2–5.5 km below seafloor and thus within the crust. However, some earthquakes were located at mantle depth and there seems to be a tendency of earthquakes occurring at greater depth in the northern portion of the network (Figure 11).

5.7. Time Evolution of Seismicity

[37] Microseismicity is generally highly variable in space and time and controlled by tectonic stresses caused by global plate motion, stresses caused by the emplacement of dykes and intrusions, and thermal cooling and contraction. The network deployed at the Logatchev Massif had the longest deployment period and is hence the only one that captured significant changes in time. Within the network, spatial pattern remained reasonable constant (Figure 10). However, temporarily the seismicity rate changed significantly between January and March 2009 (Figure 6) from ∼10 events per day in the first 5 days of the deployment to ∼20 and more events per day in late January. In mid-February, the rate was with up to 30 events per day highest, dropping below 10 earthquakes per day in March between Julian day
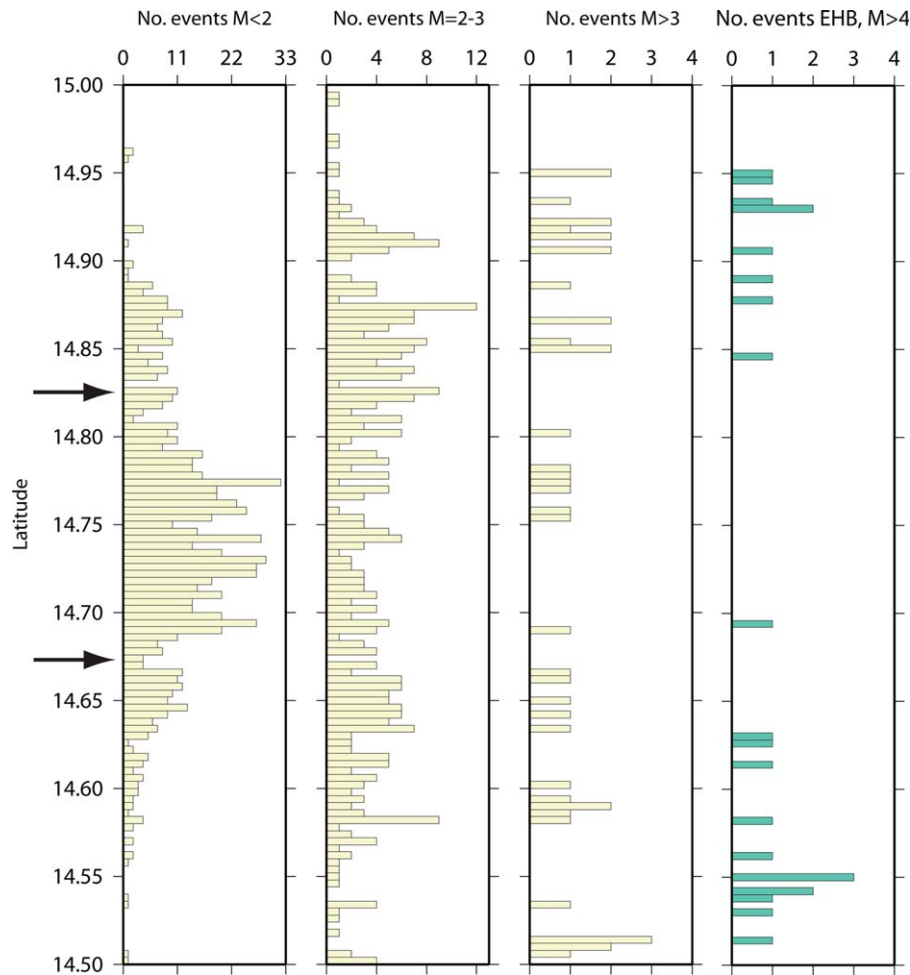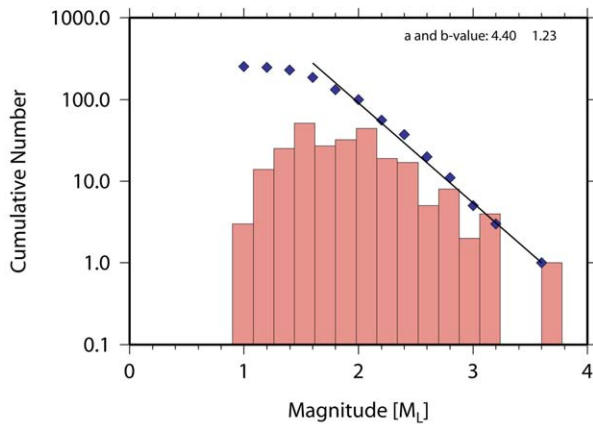
Figure 7. Deployment 3—Logatchev Massif: distribution of seismicity as a function of latitude and magnitude. Arrows mark the extent of the network. Right-hand side figure shows globally recorded events with magnitudes approximately larger M > 4 from the EHB catalog [*Engdahl et al.*, 1998; *International Seismological Centre*, 2009].

65 to 70 (Figure 6). The pattern generally did not correlate with mainshock-aftershock sequences.

[38] Just to the north of the network major seismic activity occurred at distances <5 km from the network and epicenters could be determined with high precision. Pattern of the majority of microseismicity occurred within the center of the median valley where the 30 December 2008 earthquake (M = 4.8) occurred (Figures 5 and 10). In addition, seismicity occurred at faults bounding the inner valley. This pattern was most evident in January and March. The activity within the median valley and activity at the bounding faults of the inner valley included normal faulting earthquakes, dipping at ∼30–60° (Figure 8a). At least in January, a third fault seemed to be active at the dome to the southeast of OBS05. Thus, different faults seemed to be active at the same time.

[39] Seismic activity to the south of the network mimicked the activity just discussed. Between 14.7°N and 14.55°N seismicity occurred predominantly along the central neovolcanic zone, roughly running along the 45°W meridian. In addition, seismicity was observed to the west in the deepest portion of the median valley next to the western bounding fault (Figure 10). Seismicity further south had too large errors to be conclusive. However, on 24 March a major swarm of seismicity occurred just south to 14.5°N, including two teleseismically detected earthquakes. This sequence provided clear mainshock-aftershock pattern. Aftershocks, however, are not well resolved as the network was recovered hours after the first shock hit at 11:56 UTC. Another mainshock-aftershock sequence occurred to the north on 23 January at 14.92°N, 44.93°W, following a $M_L = 3.3$ earthquake. Seismicity rapidly decayed after three days.

a) Seismicity at center of rift valley (projected along A-A')

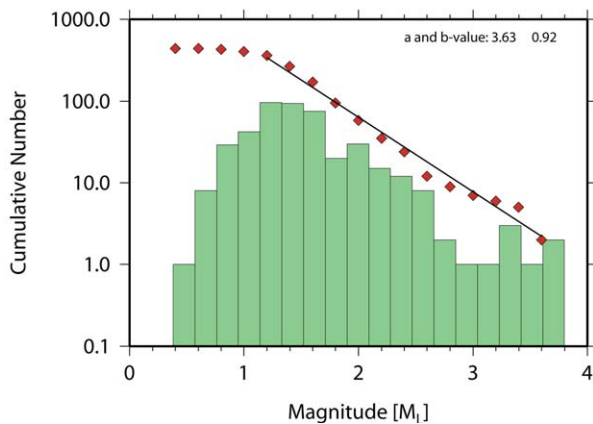b) Seismicity at Logatchev OCC (projected along C-C')

Figure 8. Deployment 3—Logatchev Massif: histograms of seismicity and *a* and *b* values for (a) median valley centered activity to the northwest of the Logaqtchev Massif (*b* = 1.2) and (b) activity at the Logatchev Massif core complex (*b* = 0.9).

6. Discussion

6.1. Distribution of Microseismicity

[40] The main features from the surveys in area-1 in the vicinity of the Ascension transform (Figure 1) are similar to most previous studies of micro-earthquakes at the MAR, indicating that most earthquakes cluster within $\pm \sim 5$ km of the ridge axis [*Toomey et al.*, 1988; *Wolfe et al.*, 1995; *Barclay et al.*, 2001; *Tilmann et al.*, 2004], leaving the flanking rift mountains seismically inactive. For the network in the Ascension intratransform segment earthquakes tended to occur near the center of the rift valley (Figure 1b). Further, some events occurred at the northeastern inside corner of the spreading segment. A similar pattern was observed at the southern Mid-Atlantic Ridge near 5°S [*Tilmann et al.*, 2004] and at the Atlantis Massif [*Collins et al.*, 2012], suggesting that inside corner settings suffer from tectonic or flexural stresses off axis. However, the southwestern inside corner of the same spreading segment remained largely inactive.

[41] At the segment to the south of the Ascension transform seismicity occurred mainly along the center of the median valley and hence zone of recent magmatic activity and thus may indicate either dyke emplacement or thermal cooling after a magmatic event. However, the lack of seismic swarms may suggest that events reflect spreading on axial valley faults rather than indicating magmatism. Interestingly, we observed a ± 15 km wide gap of seismicity centered at 7.8°S. This gap
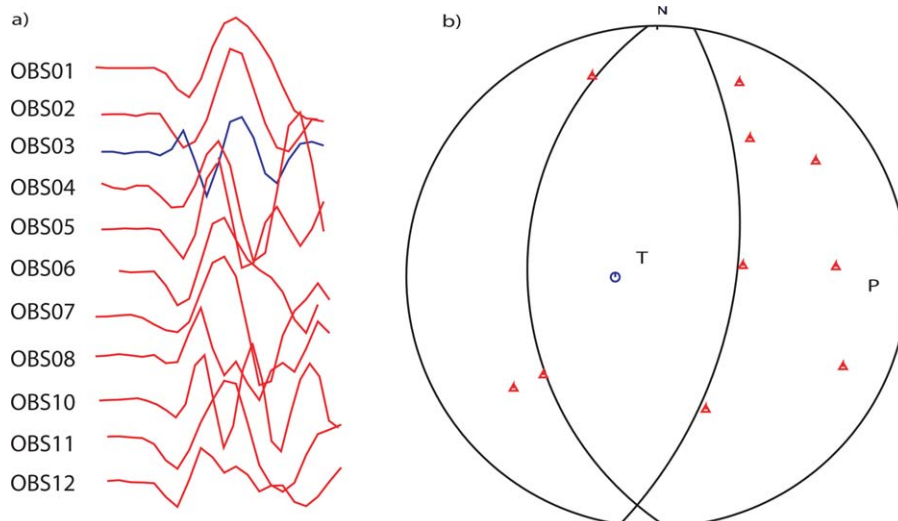

Figure 9. Deployment 3—Logatchev Massif: focal mechanism of a $M_L = 3.6$ earthquake of 3 February 2009. (a) Seismograms indicating first motions color coded by polarity; (b) focal mechanism.
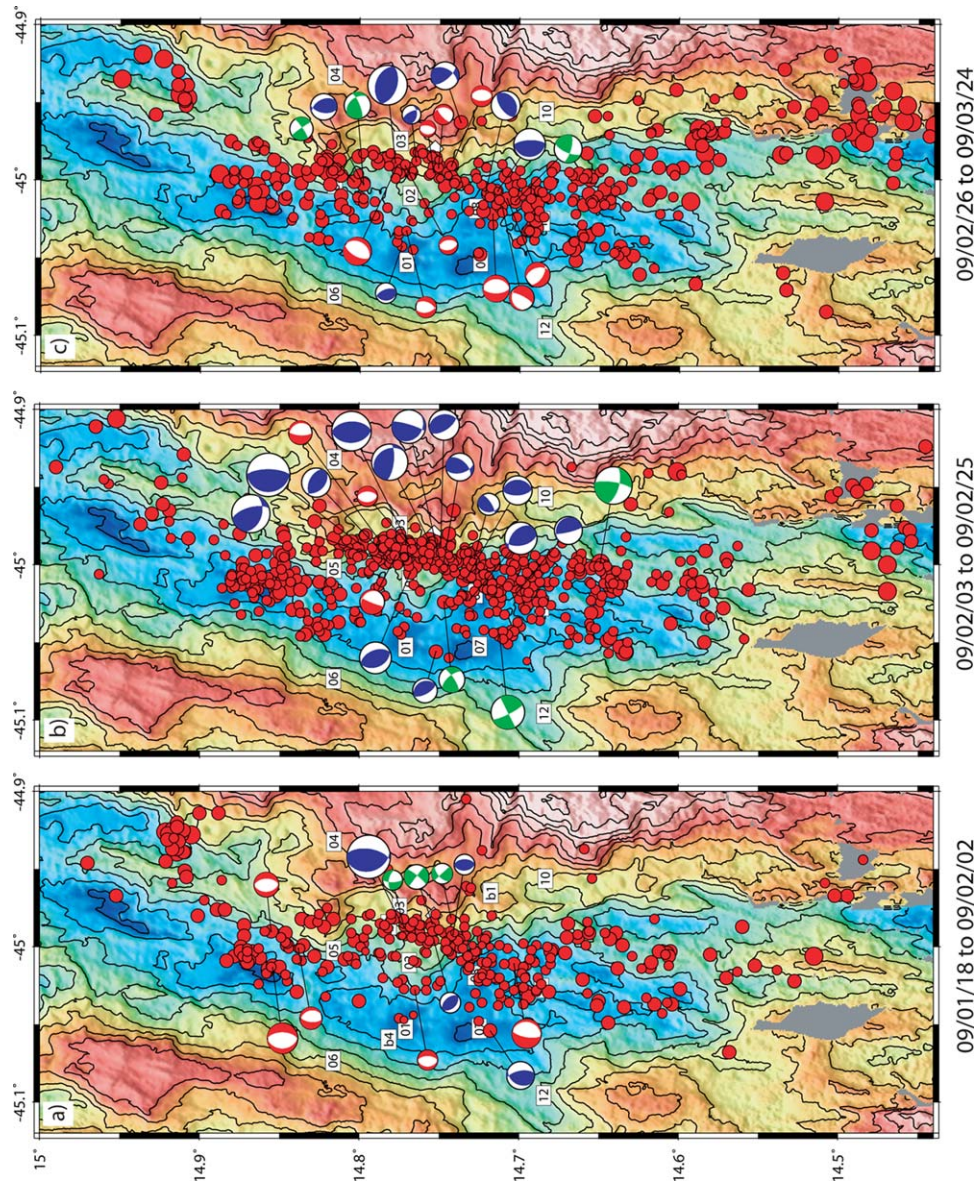
Figure 10. Deployment 3—Logatchev Massif: epicenters and focal mechanisms for local earthquakes for (a) 18 January to 2 February 2009; (b) 3–25 February 2009; (c) 26 February to 24 March 2009. Red focal mechanisms indicate normal faulting, blue thrust faulting, and green strike slip faulting.

occurred where the seabed was inflated and where the off-axis hotspot island Ascension occurs. It has been reported elsewhere that off-axis hotspots may channel material toward the ridge axis [e.g., *Ito et al.*, 2003; *Grevemeyer*, 1996], causing excess magmatism at the adjacent ridge crest. At the Mid-Atlantic Ridge near 22°N such an inflated and magmatically robust ridge segment showed a profound gap in the seismicity derived from autonomous hydrophones operated in the SOFAR channel [*Smith et al.*, 2003; *Escartín et al.*, 2008; *Dannowski et al.*, 2011]. The low level of seismicity along this segment has been confirmed by a microseismic

study [*Kahle*, 2007], suggesting that segments of excessive magmatism are characterized by thick crust and thin lithosphere [*Cannat*, 1996]. Such segments may behave like fast-spreading ridges and hence may not be able to generate large normal faulting events.

[42] The most interesting distribution of seismicity was observed in the vicinity of the Logatchev Massif (Figures 2 and 3). Geophysical and petrological data indicated that the massif, that hosts the Logatchev vent fields [e.g., *Petersen et al.*, 2009], is related to core complex formation
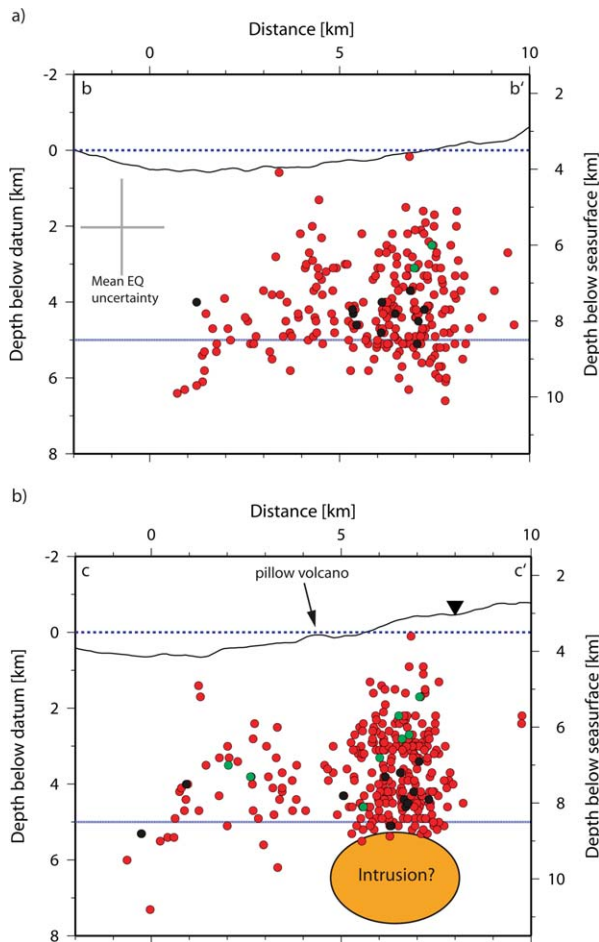
Figure 11. Deployment 3—Logatchev Massif: cross section of transects (a) b-b′ and (b) c-c′. Locations are indicated in Figure 2. We projected events ±3 km off of the profiles. Black dots indicate earthquakes with reverse faulting, green dots with normal faulting behavior. Red dots correspond to events with unresolved mechanism. Dotted blue line indicates the datum, solid blue line is the crust/mantle boundary from gravity [*Fujiwara et al.*, 2003]. Black inverted triangle mark the location of the high-temperature Logatchev vent field. Pillow volcano was described by *Petersen et al.* [2009].

[*Escartin and Cannat*, 1999; *Fujiwara et al.*, 2003]. Seismic activity in the vicinity of the massif is clearly shifted away from the inner median valley toward the eastern flanking rift mountains. Here, seismicity clusters at 5–8 km off axis and is clearly offset from the >4000 m deep median valley. In general, the location of the ridge axis at the deepest portion of the median valley is supported by magnetic data, providing a well-defined magnetic high [*Fujiwara et al.*, 2003]. However, in the southern portion of the segment S2 next to the Logatchev vent field magnetic pattern are less well defined [*Fujiwara et al.*, 2003], though. Further away from the proposed core complex seismicity

clustered again in the vicinity of the center of inner median valley (Figures 3 and 5), suggesting that the observed seismicity pattern at the OCC are a local phenomenon rather indicating an eastward deviation of the spreading axis. The Logatchev hydrothermal vent field occurs just eastward of the zone of major seismicity, suggesting a relationship between the occurrence of faulting, microearthquakes, and hydrothermal venting.

[43] In the past, spreading at the Logatchev segment S2 to the south of the 15°20′FZ [*Fujiwara et al.*, 2003] was asymmetric with a faster rate toward the east. The degree of asymmetry reported by *Fujiwara et al.* [2003] was rather small, with 12.2 ± 0.5 km/Ma toward the east and 12.8 ± 0.6 km/Ma toward the west. Other core complexes indicated much stronger degrees of asymmetric spreading, like the Atlantis Massif at the Mid-Atlantic Ridge (~100%) [*Grimes et al.*, 2008] and the Atlantic Bank (~80%) at the South West Indian Ridge (SWIR) [*Baines et al.*, 2008]. For the Atlantis Massif *Collins et al.* [2012] found that seismicity showed the tendency to occur near the western bounding fault, but still predominantly within the inner median valley. Seismicity for the Logatchev segment S2, however, is clearly asymmetric, supporting the idea that the plate boundary fault is currently shifted eastward, suggesting that asymmetric spreading and asymmetric distribution of seismicity are not necessarily correlated with each other.

[44] Monitoring of the seismicity at the Mid-Atlantic Ridge using autonomous hydrophone arrays suggested that core complexes and inside corner highs are seismically more active than segment centers [*Escartín et al.*, 2008]. This pattern was consistent with previous results from two microearthquake studies, suggesting that seismicity may occur at or below two inside corner highs at 34°40′N [*Barclay et al.*, 2001] and at 28°55′N [*Wolfe et al.*, 1995] rather than at the center of the median valley. However, these earthquakes occurred outside of the networks and hence had large location errors. The first dedicated microearthquake study of a core complex was conducted at the TAG detachment near 26°8′N [*deMartin et al.*, 2007], where most seismicity was rooted in the neovolcanic zone and hence in the inner median valley. A second survey was conducted at the Atlantis Massif; major seismicity occurred within the median valley. However, some activity occurred within the core complex and focal mechanism suggested both normal faulting and strike-slip faulting [*Collins et al.*, 2012], indicating that the

massif suffers from some tectonic stresses after it was rafted off axis. Nevertheless, the microseismicity study at the Atlantis Massif did not support the observations based on the hydroacoustic event locations, which had suggested that the massif itself was the source area of profound seismicity with magnitudes of >2.5 [*Williams et al.*,2006; *Collins et al.*, 2012]. For the area in the vicinity of the Logatchev vent field seismicity based on hydrophones moored in the SOFAR channel occurred predominantly at the massif to the east of the main vent site [*Escartín et al.*, 2008]. Thus, hydroacoustically detected seismicity was, with respect to the seismicity located with our local network, offset toward higher topography. We thus observed features similar to those reported by *Collins et al.* [2012]. This may either indicate that hydrophone-recorded data might be biased, indicating an offset between the epicenter and the T-wave entry point into the SOFAR channel, as suggested by *Williams et al.* [2006], or different pattern might be related to time-space evolution of seismicity. In any case, the microearthquake survey at the Logatchev Massif is one of the first studies outlining that major tectonic activity and faulting is active at the flanking rift mountains in the vicinity of a core complex. Previously, *deMartin et al.* [2007] reported antithetic normal faulting to the east of the TAG vent field.

6.2. Distribution of Large Teleseismic Earthquakes

[45] The four teleseismic earthquakes recorded at our network during operation all occurred within the inner median valley of the MAR. Similar features were observed before at other spreading segments. *Kong et al.* [1992] captured a swarm of five earthquakes located by the ISC with an ocean floor network at the Mid-Atlantic Ridge near 26°N. All globally recorded events occurred roughly 25 km to the south of the network, and a large number of aftershocks ruptured within the center of the median valley. At the Mid-Atlantic Ridge near 30°N, *Collins et al.* [2012] detected with their network two large mainshock-aftershock sequences that included five teleseismic earthquakes. The mainshock and aftershocks occurred on the western side of the median valley and close to the intersection of an adjacent transform fault. However, they occurred within the median valley and not under the flanking rift mountains.

[46] The observation that large earthquakes at slow-spreading ridges tend to occur in the median

valley is supported by waveform inversion studies of mid-ocean ridge normal faulting earthquakes of magnitudes ∼5.5 or larger recorded at teleseismic distances. To constrain the epicentral region, water column reverberations occurring in the waveform data were used. To fit the reverberations these large earthquakes had to occur beneath the relatively deep inner floor of the median valley rather than beneath the shallower rift mountains [e.g., *Huang et al.*, 1986; *Huang and Solomon*, 1988]. Along with the microseismicity constrained by the networks it seems reasonable to suggest that all major seismicity at slow-spreading ridges occurs within the median valley and perhaps at the first bounding fault on either side of the rift valley. However, older faults seem to be largely inactive.

6.3. Frequency-Size Distribution of Earthquakes

[47] An interesting feature of seismicity was the observation that the number of magnitude 2–3 earthquakes seem to increase away from the Logatchev Massif core complex (Figure 7). It might be reasonably to hypothesize that this feature is related to tectonics of the core complex. The Logatchev field vent fluids [*Bogdanov et al.*, 1997] and alteration of rocks [*Augustin et al.*, 2012] indicate that the Logatchev field occurs in a serpentinite hosted setting. Serpentinites provide low friction coefficients [*Escartín et al.*, 1997] and hence might support frequent and small earthquakes that release only small amounts of stress. In stronger rocks, larger stresses can be accumulated and larger earthquakes occur. The size distribution may therefore be used to discriminate between strong and weak faults. In the trench-outer rise area off Nicaragua bending-related faulting promoted mantle serpentinization [*Grevemeyer et al.*, 2007; *Ivandic et al.*, 2008]. The *b* value for the area not yet affect by serpentinization was in the order of 0.7 while the area affected by serpentinization provided a *b* value of 2.7 [*Lefeldt et al.*, 2009]. The asymmetric distributed seismicity in the vicinity of the Logatchev Massif indicated a *b* value of 0.9 (Figure 8), while the symmetric seismicity focusing at the center of the median valley provided and a *b* value of 1.2. Thus, *b* values do not support serpentinization. In contrast, both estimates range within the values reported for the MAR [e.g., *Kong et al.*, 1992].

[48] Globally recorded events, however, provide evidence that the area of the Logatchev Massif indicates a profound deficit of earthquakes M>4. To survey the distribution of teleseismically

recorded earthquakes we used EHB relocated earthquakes [*Engdahl et al.*, 1998; *International Seismological Centre*, 2009], providing relocations of globally recorded seismic events using corrections accounting for three-dimensional inhomogeneity's of Earth's structure. For the MAR to the south of the 15°20′N transform fault the EHB catalogue provided 27 earthquakes occurring between 1968 and 2002. The resulting distribution of globally located earthquakes supports the pattern of the $M > 2$ earthquakes detected with the local network (Figure 7). Thus, only one of the 27 events hitting the area occurred in the vicinity of the Logatchev core complex but most events clearly occurred to its south and north. Even though the b value seemed to be dominated by other processes the lack of $M \sim 4$ events within the vicinity of the Logatchev Massif may suggest that faults in the area are rather weak. This feature is consistent with the observation that mainshock-aftershock sequences reported in hydroacoustic catalogues yielded faster decay rates for asymmetric segments with detachment faults, while normal faulting mainshock-aftershock sequences at symmetric spreading segments yielded slower decay rates [*Simao et al.*, 2010]. This dependence was suggested to be controlled by the weak rheology of detachment faults relative to the rheology found at segments supporting symmetric and more magmatic spreading [*Simao et al.*, 2010]. On the other hand lithosphere might be rather thin. Observations indicated that high-temperature fluids of the Logatchev vents require some magma somewhere in the system, most probably directly below the vent field. The heat source may locally thin the brittle layer and restrict the earthquakes to the shallowest crust.

[49] At the TAG segment near 26°N *Kong et al.* [1992] found higher b values of 1.1–1.5 near the segment center and lower values of 0.6–0.9 near the tectonically dominated segment ends. Higher b values indicate a larger proportion of smaller earthquakes and are a characteristic feature of magmatically active regions where b as a function of M_0 often exceeds the global average of 0.7 by a factor of 2 [e.g., *Wyss et al.*, 1997]. Our b value of 0.9 therefore supports a setting governed by tectonics and cooling stresses rather than active magma injection. This conclusion is in agreement with results of *Tilmann et al.* [2004] at the MAR near 5°S, where they reported a b value of 0.8 for a tectonically dominated setting. The b value of 1.2 occurring to the northwest of the Logatchev Massif agrees with values reported for segment centers elsewhere [*Kong et al.*, 1992].

[50] The area to the northwest of the Logatchev Massif was hit on 30 December 2008 by a $M = 4.8$ earthquake. *Rubin and Pollard* [1988] suggested for Iceland and Afar that dyke emplacement within the median valley may trigger normal faulting at the adjacent bounding faults. Therefore, the observed pattern, including activity within the center of the median valley and at the adjacent off-axis bounding faults, may indicate dyke emplacement. For the clustered activity in the median valley we obtained a magnitude of completeness of 1.9 and a b value of 1.2 (Figure 8). However, based on b value mapping elsewhere, magmatically active setting are expected to be characterized by much larger b values [e.g., *Wyss et al.*, 1997]. We are therefore confident that the seismic activity is related to tectonic stresses rather than magmatism. Thus, the $M = 4.8$ 30 December 2008 earthquake may have caused static changes of Coulomb stresses that loaded adjacent faults [*King et al.*, 1994], causing activity at nearby faults following the mainshock.

6.4. Focal Mechanisms

[51] At slow-spreading mid-ocean ridges, we would expect two forms of focal mechanisms: (i) normal faulting indicative of extension and rift valley formation and (ii) transfer or strike-slip faulting at ridge crest discontinuities and near-transform fault boundaries [e.g., *Sykes*, 1967]. Normal faulting is a well-understood and described process and is clearly documented by teleseismic earthquakes [e.g., *Huang et al.*, 1986; *Huang and Solomon*, 1988] and local microseismicity surveys at the Mid-Atlantic Ridge [e.g., *Kong et al.*, 1992; *Barclay et al.*, 2001]. In addition, local seismicity surveys reported compressional earthquakes and hence reverse faulting unknown from the global record [e.g., *Kong et al.*, 1992; *Wolfe et al.*, 1995]. The compressional events were interpreted to be related to along axis variations of thermal stresses caused by cooling. For the Mid-Atlantic Ridge at 26°N, *Kong et al.* [1992] suggested, from a three weeks OBS deployment conducted in summer 1985, that cooling of a relatively recent intrusion was associated with thermal stresses and fracturing in the immediately surrounding crust, accounting for areas of intense earthquake activity, a diversity of focal mechanisms (including reverse faulting), and the presence of a high-temperature hydrothermal vent field. Overall, features reported by *Kong et al.* [1992] are similar to our observations.

[52] In addition to the thermal cooling stresses envisioned by *Kong et al.* [1992] and *Wolfe et al.*

[1995], dyke emplacement may cause reverse faulting. In Iceland, microearthquakes outlined a progressive melt intrusion of a dyke moving upward [*White et al.*, 2011]. Moment tensors indicated double-couple failure, with fault mechanisms sometimes flipping between normal and reverse faulting. However, in our data we neither observed clear migration pattern in the well-located seismicity nor flipping of sense of faulting within minutes.

[53] Subsidence after drainage of a magma reservoir is another mechanism that may cause reverse faulting. To explain compressional focal mechanisms from the Bardarbubga volcano in Iceland, *Nettles and Ekström* [1998] suggested that deflation of a magma chamber increased horizontal compression, so that the roof block above the magma chamber subsided with respect to the surrounding rock.

[54] At the Juan de Fuca Ridge, a large number of thrust faulting earthquakes have been linked to the presence of a crustal magma chamber. Earthquake focal mechanisms, however, revealed a transition from normal faulting above the crustal magma reservoir to reverse faulting on either flank [*Wilcock et al.*, 2009]. In contrast, at the Logatchev Massif we did not observe any pattern that may resemble the distribution of focal mechanisms caused by stresses related to emplacement of pressurized magma as modeled by *Wilcock et al.* [2009].

[55] Dredging of the Logatchev Massif and drilling results from IODP leg 209 at site 1270 support that the domal high is largely composed of mantle rocks [*Shipboard Scientific Party*, 2004; *Petersen et al.*, 2009]. Thus, serpentinization might be an alternative mechanism causing reverse faulting, because it is an exothermic reaction that is accompanied by volume expansion. Consequently, serpentinization may cause compression and hence reverse faulting at the edge of the expanding zone.

[56] In a cross section through the band of seismicity to the west of the Logatchev Massif (Figure 11), microearthquakes are rather randomly distributed and did not support clear fault structures. Random pattern of seismicity would support both cooling of an intrusive body by hydrothermal circulation in a highly fractured media and volume expansion by serpentinization. In addition to reverse faulting, *Kong et al.* [1992] reported a diversity of focal mechanisms favoring cooling, while our data basically showed two dominating mechanisms: shallow normal faulting and reverse faulting at greater depth. Thus, virtually all normal

faulting events occurred at a depth of 1.5–4 km below datum, while all compressional events ruptured at 3.5–5.5 km below datum. Further, reverse faulting earthquakes are larger than the normal faulting event. Thus, shallow normal faulting might be a response to volume expansion at depth. We suggest that volume expansion rather than cooling controls the seismicity pattern of the Logatchev Massif.

[57] In addition to the random pattern of seismicity, normal faulting earthquakes near the Logatchev hydrothermal vent field showed common features, including faults dipping at 50–60°. Thus, focal mechanisms do not support any shallow dipping detachment. However, overall seismicity patterns have to be interpreted carefully as 95% confidence intervals translate to errors of ± 0.5–2 km in profile direction and ± 1–2 km in depth.

6.5. Depth Distribution of Microearthquakes

[58] Microearthquakes at the Mid-Atlantic Ridge generally do not occur right below the seabed but 2–3 km deeper. In most cases, earthquakes occurred at depth ranges of 2–7 km below the seafloor and the majority of earthquakes ruptured within the lower crust [*Toomey et al.*, 1988; *Wolfe et al.*, 1995; *Collins et al.*, 2012]. These observations from previous studies are supported by our observations, revealing that most microearthquakes occur at 3–6 km depth. At magmatically robust settings, however, microearthquakes occurred at shallower depth. *Barclay et al.* [2001] reported results from an experiment at a dome-like high near 35°N at the MAR and found that seismicity clustered at 3–4 km depth. A similar dome-like feature can be observed in area-1 at the MAR near 7.8°S, where deployment 2 provided events at 2–4 km depth, averaging at $\sim$3 km depth (Table 1). Both settings, the MAR at 35°N and the MAR at $\sim$7.8°S, have similar dome-shaped bathymetric highs at the segment center. Thus, it seems to be that morphology can be used as first-order approximation, constraining the thermal state of a ridge segment.

[59] In contrast, *Tilmann et al.* [2004] found that seismicity at 5°S of the MAR, where an inside corner high has been rifted apart [*Reston et al.*, 2002], occurred in the lower crust and predominantly within the uppermost mantle at a depth of 5–8 km below seafloor in lithosphere with a crustal thickness of 3–4 km. Faults associate with these earthquakes may act as conduits for seawater to serpentinize the mantle.

[60] The depth distribution of microearthquakes can be an agent to approximate the temperature structure at depth. Thus, the occurrence of microseismicity indicates that temperatures support a brittle regime and hence temperatures of roughly <600°C [e.g., *Wilcock et al.*, 2002; *Golden et al.*, 2003]. Further, temperatures of ~600°C represent the upper temperature limit for serpentinization, consistent with the occurrence of reverse faulting at 3–5 km depth, indicating expansion caused by serpentinization. This idea is further supported by the end-member compositions of the hydrothermal fluids, indicating very high concentrations of dissolved methane and hydrogen which are generally related to serpentinization [*Bogdanov et al.*, 1997; *Schmidt et al.*, 2007]. Thus, the seismically active region just to the west of the Logatchev hydrothermal vent field may outline a crustal volume that is effectively ventilated by hydrothermal fluids. Hydrothermal circulation might be facilitated by the exothermic reaction of peridotite and water to serpentine. However, a number of studies indicated that energy from exothermic serpentinization is not enough to drive high-temperature venting [e.g., *Allen and Seyfried*, 2004]. Such results are corroborated by the fact that talc alteration indicated that Si metasomatism overprinted serpentinization and hence may indicate the presence of gabbroic intrusions at greater depth below the Logatchev vent field [*Augustin et al.*, 2012].

6.6. Conceptual Model for Hydrothermal Venting at the Logatchev Massif

[61] The Logatchev hydrothermal vent field occurs just eastward of a major cluster of microearthquakes at 2–5 km depth. Hydrothermal activity is most prominent along a 800 m long zone striking roughly NW-SE [*Petersen et al.*, 2009] and occurs approximately 8 km off the median valley defined by magnetic and swath-mapping [*Fujiwara et al.*, 2003]. The main vent sites are located on a plateau right below a 350 m high cliff between 3060 and 2910 m water depth. There are abundant outcrops of serpentinite and gabbroic rocks at the eastern rift mountains; upper crustal rocks are less abundant at the rift walls but dominate the median valley floor [*Petersen et al.*, 2009]. Two distinctive types of vents with high-temperature hydrothermal discharge were described [*Petersen et al.*, 2009]: (i) black smoker-type vents with fluid temperatures of up to 330°C and (ii) so-called "smoking craters" with higher fluid temperatures of up to 360°C, discharging from local depressions. Further, a number of diffuse hydrothermal sites were found, discharging fluids at much lower temperatures. End-member compositions of the hydrothermal fluids are characterized by very high concentrations of dissolved methane and hydrogen (up to 3.5 and 19 mM, respectively), which relate to subsurface serpentinization processes [*Bogdanov et al.*, 1997; *Schmidt et al.*, 2007].

[62] Alteration of peridotites suggested that mineral mobilization (e.g., Cu) occurred at temperatures of >>350°C at depth [*Augustin et al.*, 2012]. However, the enrichment of serpentinite and lizardite separates in trace elements such as Sr, Rb, Ba, U, and Pb indicated a considerable degree of interaction with ambient seawater. Further, δ^{18}O formation temperatures of secondary minerals are considerably lower than temperatures of black smoker fluids, supporting extensive fluid mixing and/or reequilibration of host rocks with ambient seawater [*Augustin et al.*, 2012]. Interestingly, the occurrences of talc alteration showed that Si metasomatism overprinted serpentinization and hence may indicate the impact of gabbroic intrusions [*Augustin et al.*, 2012]. However, in the vicinity of a gabbroic intrusion temperatures may have been too great for serpentinization as talc is stable at much higher temperatures. Thus, gabbros may have been intruded at a depth of >5–6 km within the mantle, as envisioned by *Cannat* [1996].

[63] *Petersen et al.* [2009] suggested that the vents are fed from a deeper magma source or intrusive body within the eastern portion of the median valley that is tapped by a listric normal fault. This fault is suggested to be steep at shallow depth, turning into a low-angle fault at depth. Such a scenario is opposite to the setting proposed for feeding and controlling the detachment fault at the TAG hydrothermal vent site at 26°8′N [*deMartin et al.*, 2007], where the fault dips at 60–70° at the median valley, rolling over and forming an inactive low-angle fault off axis [e.g., *Reston and Ranero*, 2011]. In both cases, the heat source is displaced by some ~5 km from the vents toward the ridge axis. Microseismicity at the Logatchev vent field, however, supports a different scenario. We suggest that the major cluster of microearthquakes occurring nearly below the Logatchev vents may indicate volume expansion caused by serpentinization. However, the focused pattern of seismicity may suggest that a magmatic heat source occurs at the toe or below the cluster of major seismicity, similar to the features detected by *Wilcock et al.* [2009] at the Juan de Fuca Ridge where seismicity was triggered by stresses cause by intrusion of pressurized magma. It is interesting

to notice that such a heat source would occur below a pillow volcano detected by *Petersen et al.* [2009] and thus might have fed the volcano recently (Figure 11).

[64] The zone of proposed serpentinization occurred near the crust-mantle boundary as defined by gravity data [*Fujiwara et al.*, 2003], and hence microearthquakes tended to occur within a depth range generally attributed to the crust and uppermost mantle; thus, the majority of events may represent crustal events. Earthquakes are generally restricted to the brittle lithosphere. For mid-ocean ridges, temperatures of approximately 600°C define the highest temperature where earthquakes occur [e.g., *Wilcock et al.*, 2002; *Golden et al.*, 2003]. Thus, the seismicity patterns suggest that temperatures of 500–600°C occur at 5–6 km below datum (9–10 km below sea surface), indicating that the entire crust supports brittle failure and hence faulting and perhaps seawater migration and hydrothermal recharge down to mantle depth. In the vicinity of the Logatchev vent field, we observed a number of normal faulting events. We suggest that normal faulting in the vicinity of the vents facilitates focused discharge of hydrothermal fluids and is controlling the surface location of venting. At shallower depth, approximately <2 km below the seabed, we do not observe any microearthquakes. At such a shallow depth, a network of faults and fractures in the highly porous upper crust may just support very small seismic events that were below the detection threshold. Further, the highly porous and permeable uppermost crust may allow shallow seawater recharge, explaining $\delta^{18}O$ formation and low-temperature alteration pattern [*Augustin et al.*, 2012]. This scenario may control shallow seismicity at 2–3 km depth.

[65] The temperature of >600°C deduced for the mantle has important implications, because serpentinization shows profound kinematics and is temperature dependent [*Martin and Fyfe*, 1970; *Iyer et al.*, 2012]. Thus, serpentinization is most efficient at a temperature of ∼270°C [*Martin and Fyfe*, 1970] and reaction speed is reduced toward higher and lower temperatures; the 600°C temperature presents the thermal depth limit to serpentinization. Therefore, serpentinization, as indicated by fluid venting at the Logatchev field [e.g., *Bogdanov et al.*, 1997; *Schmidt et al.*, 2007], is unlikely to occur at mantle depth of >5 km as estimated from gravity data [*Fujiwara et al.*, 2003], but has to occur within the massif itself. Drilling results from IODP leg 209 at site 1270 support

that the Logatchev Massif is largely composed of mantle rocks [*Shipboard Scientific Party*, 2004]. This feature supports that reverse faulting is indeed caused by volume expansion within the massif. Further, energy released by serpentinization may facilitate hydrothermal circulation. However, to fuel a high-temperature circulation system like the Logatchev field, the energy provided by serpentinisation is not high enough [e.g., *Allen and Seyfried*, 2004]. Thus, some magmatic component is needed. Indeed, talc alteration indicated that Si metasomatism overprinted serpentinization and thus supports the presence of gabbroic intrusions in the vicinity of the Logatchev vent field [*Augustin et al.*, 2012]. We suggest that the magmatic intrusion is located below the cluster of intense seismicity to the west of the Logatchev field (Figure 11).

[66] Further, at the Logatchev Massif focal mechanisms indicate two sets of faults (Figure 8). Both can also be deduced from bathymetry. The first set represents the normal faults that form the flanking rift mountains. In addition, the massif is cut by a number of transfer or strike-slip faults. Two well-resolved strike-slip earthquakes occurred in January (Figure 10a). One of the events ruptured just to the west of the Logatchev vent field and the strike of the inferred NW-SE trending fault roughly approximates the strike of the vent field. A second strike-slip event occurred just south of the vent field. It might therefore be reasonable to suggest that the location of the vent field is controlled by two intersecting faults. Similar features have been observed at other nontransform offsets hosting core complexes and hydrothermal vent sites to the south of the Azores [*Gracia et al.*, 2000]. Thus, the pervasive normal and localized strike-slip faulting taking place at segment ends and nontransform offsets may nurture enhanced fluid circulation and favor serpentinization and high-temperature hydrothermal venting.

6. Conclusions

[67] Three microseismicity surveys were conducted at the Mid-Atlantic Ridge. Two experiments studied the MAR at 7°S to 8°15'S, including a 13 day experiment that sampled the seismicity in a 20 km wide segment sandwiched between the double Ascension transform fault and a 24 day long deployment to the south of the Ascension transform fault. The networks provided on the order of 210 and 120 located

microearthquakes, respectively. Microearthquakes cluster along the median valley and focal depths of all events range between 2 and 7 km below the seafloor. Events tended to be deeper in the northern segment (3–6 km) sandwiched between the double Ascension transform fault and shallow in the southern segment (2–4 km), which seems to be magmatically more robust. The deployments should have been able to detect seismicity from three inside corner massifs. Only the northernmost massif showed some minor seismicity. In general, however, the inside corner massifs were seismically quiet.

[68] The third experiment was conducted at the massif that hosts the Logatchev hydrothermal site, a serpentinite hosted vent field [*Bogdanov et al.*, 1997; *Schmidt et al.*, 2007] at the MAR between 14°40′N and 14°50′N, and recorded the local seismicity for 67 days. In total, on the order of 1600 events were located. To the north and to the south of the massif, seismicity was concentrated along the median valley and the neovolcanic zone. At the massif, however, seismic activity was clearly shifted by 5–8 km away from the ridge axis and occurred under the flanking eastern rift mountains. The Logatchev high-temperature vent field occurs just to the east of the seismically active zone. Focal depths of the earthquakes ranged from 1.5 to 5.5 km. Some of the deeper events at 3.5–5.5 km depth showed reverse faulting. We believe that reverse faulting is related either to the injection of magma into a sill causing thermal stresses and fracturing in its vicinity or it is related to volume expansion caused by serpentinization. At shallower depths of 1.5–4 km, a number of earthquakes in the vicinity of the vent field showed normal faulting. Normal faulting may facilitate focused fluid flow and fluid discharge, feeding the vent field. Further, a second set of faults occurs, running roughly perpendicular to the normal faults. Cross-cutting faults may govern the surface location of the vent field.

Acknowledgments

References

Allen, D. E., and W. E. Seyfried (2004), Serpentinization and heat generation: Constraints from Lost City and Rainbow hydrothermal systems, *Geochim. Cosmochim. Acta*, *68*, 1347–1355.

Augustin, N., H. Paulick, K. S. Lackschewitz, A. Eisenhauer, D. Garbe-Schönberg, T. Kuhn, R. Botz, and M. Schmidt (2012), Alteration at the ultramafic-hosted Logatchev hydrothermal field: Constraints from trace element and Sr-O isotope data, *Geochem. Geophys. Geosyst.*, *13*, Q0AE07, doi:10.1029/2011GC003903.

Baines, A. G., M. J. Cheadle, B. E. John, and J. J. Schwartz (2008), The rate of oceanic detachment faulting at Atlantis Bank, SW Indian Ridge, *Earth Planet. Sci. Lett.*, *273*(1–2), 105–114, doi:10.1016/j.epsl.2008.06.013.

Barclay, A. H., D. R. Toomey, and S. C. Solomon (2001), Microearthquake characteristics and crustal Vp/Vs structure at the Mid-Atlantic Ridge, 35°N, *J. Geophys. Res.*, *106*, 2017–2034, doi:10.1029/2000JB900371.

Bogdanov, Y. A., N. S. Bortnikov, I. V. Vikentev, E. G. Gurvich, and A. M. Sagalevich (1997), A new type of modern mineral-forming system: Black smokers of the hydrothermal field at 14°45′N latitude, Mid-Atlantic Ridge, *Geol. Ore Deposit*, *39*(1), 58–78.

Brozena, J. M., and R. S. White (1990), Ridge jumps and propagations in the South Atlantic Ocean, *Nature*, *348*, 149–152.

Bruguier, N. J., T. A. Minshull, and J. M. Brozena (2003), Morphology and tectonics of the Mid-Atlantic Ridge, 7–12, *J. Geophys. Res.*, *108*(B2), 2093, doi:10.1029/2001JB001172.

Canales, J. P., J. A. Collins, J. Escartin, and R. S. Detrick (2000), Seismic structure across the rift valley of the Mid-Atlantic Ridge at 23_200N (MARK area): Implications for crustal accretion processes at slow spreading ridges, *J. Geophys. Res.*, *105*, 28,411–28,425.

Cann, J. R., et al. (1997), Corrugated slip surfaces formed at ridge-transform intersections on the Mid-Atlantic Ridge, *Nature*, *385*, 329–332, doi:10.1038/385329a0.

Cannat, M. (1996), How thick is the magmatic crust at slow spreading ridges? *J. Geophys. Res.*, *101*(B2), 2847–2857, doi:10.1029/95JB03116.

Collins, J. A., D. K. Smith, and J. J. McGuire (2012), Seismicity of the Atlantis Massif detachment fault, 30°N at the Mid-Atlantic Ridge, *Geochem. Geophys. Geosyst.*, *13*, Q0AG11, doi:10.1029/2012GC004210.

Dannowski, A., I. Grevemeyer, C. R. Ranero, G. Ceuleneer, M. Maia, J. P. Morgan, and P. Gente (2010), Seismic structure of an oceanic core complex at the Mid-Atlantic Ridge, 22°19′N, *J. Geophys. Res.*, *115*, B07106, doi:10.1029/2009JB006943.

Dannowski, A., I. Grevemeyer, J. Phipps Morgan, C. R. Ranero, M. Maia, and G. Klein (2011), Crustal structure of the propagating TAMMAR ridge segment on the Mid-

Atlantic Ridge, 21.5°N, *Geochem. Geophys. Geosyst.*, *12*, Q07012, doi:10.1029/2011GC003534.

deMartin, B. J., R. A. Reves-Sohn, J. P. Canales, and S. E. Humphris (2007), Kinematics and geometry of active detachment faulting beneath the TAG hydrothermal field on the Mid-Atlantic Ridge, *Geology*, *35*(8), 711–714, doi:10.1130/G23718A.1.

Engdahl, E. R., R. van der Hilst, and R. Buland (1998), Global teleseismic earthquake relocation with improved travel times and procedures for depth determination, *Bull. Seismol. Soc. Am.*, *88*, 722–743.

Escartín, J., G. Hirth, and B. Evans (1997), Effects of serpentinization on the lithospheric strength and the style of normal faulting at slow-spreading ridges, *Earth Planet. Sci. Lett.*, *151*(3–4), 181–189, doi:10.1016/S0012-821X(97)81847-X.

Escartin, J., and M. Cannat (1999), Ultramafic exposures and the gravity signature of the lithosphere near the Fifteen-Twenty Fracture Zone (Mid-Atlantic Ridge, 14°–16.5°N), *Earth Planet. Sci. Lett.*, *171*, 411–424.

Escartín, J., D. K. Smith, J. Cann, H. Schouten, C. H. Langmuir, and S. Escrig (2008), Central role of detachment faults in accretion of slow-spreading oceanic lithosphere, *Nature*, *455*, 790–794, doi:10.1038/nature07333.

Fujiwara, T., J. Lin, T. Matsumoto, P. Keleman, B. Tucholke, and J. Casey (2003), Crustal evolution of the Mid-Atlantic Ridge neat the Fifteen-Twenty fracture zone in the least 5 Ma, *Geochem. Geophys. Geosyst.*, *4*(3), 1024, doi:10.1029/2002GC000364.

Golden, C. E., S. C. Webb, and R. A. Sohn (2003), Hydrothermal microearthquake swarms beneath active vents at Middle Valley, northern Juan de Fuca ridge, *J. Geophys. Res.*, *108*(B1), 2027, doi:10.1029/2001JB000226.

Goldstein, P., D. Dodge, M. Firpo, and L. Minner (2003), SAC2000: Signal processing and analysis tools for seismologists and engineers, in *International Handbook of Earthquake and Engineering Seismology, Part B, The International Geophysics Series*, vol. 81, edited by W. H. K. Lee et al., pp. 1613–1614, Academic, London.

Gracia, E., J. C. Charlou, J. Radford-Knoery, and L. M. Parson (2000), Non-transform o¡sets along the Mid-Atlantic Ridge south of the Azores (38°N to 34°N): Ultramafic exposures and hosting of hydrothermal vents, *Earth Planet. Sci. Lett.*, *177*, 89–103.

Grevemeyer, I. (1996), Hotspot-ridge interaction in the Indian Ocean: Constraints from Geosat/ERM altimetry, *Geophys. J. Int.*, *126*, 796–804.

Grevemeyer, I., C. R. Ranero, E. R. Flueh, D. Kläschen, and J. Bialas (2007), Passive and active seismological study of bending-related faulting and mantle serpentinization at the Middle America Trench, *Earth Planet. Sci. Lett.*, *258*, 528–542, doi:10.1016/j.epsl.2007.04.013.

Grimes, C. B., B. E. John, M. J. Cheadle, and J. L. Wooden (2008), Protracted construction of gabbroic crust at a slow spreading ridge: Constraints from 206Pb/238U zircon ages from Atlantis Massif and IODP Hole U1309D (30°N, MAR), *Geochem. Geophys. Geosyst.*, *9*, Q08012, doi:10.1029/2008GC002063.

Hardebeck, J. L., and P. M. Shearer (2002), A new method for determining first-motion focal mechanisms, *Bull. Seismol. Soc. Am.*, *92*, 2264–2276, doi:10.1785/0120010200.

Havskov, J., and L. Ottemöller (2000), SEISAN earthquake analysis software, *Seismol. Res. Lett.*, *70*, 532–534.

Havskov, J., and L. Ottemöller (2010), *Routine Data Processing in Earthquake Seismology*, 347 pp., Springer.

Huang, P., and S. C. Solomon (1988), Centroid depths of mid-ocean ridge earthquakes: Dependence on spreading rate, *J. Geophys. Res.*, *93*, 13,445–13,477, doi:10.1029/JB093iB11 p13445.

Huang, P. Y., S. C. Solomon, E. A. Bergman, and J. L. Nablek (1986), Focal depth and mechanisms of Mid-Atlantic Ridge earthquakes from body wave inversion, *J. Geophys. Res.*, *91*, 579–598.

International Seismological Centre (2009), *EHB Bulletin*, Int. Seismol. Cent., Thatcham, U. K. [Available at http://www.isc.ac.uk.].

Ito, G., J. Lin, and D. Graham (2003), Observational and theoretical studies of the dynamics of mantle plume-mid-ocean ridge interaction, *Rev. Geophys.*, *41*(4), 1017, doi:10.1029/2002RG000117.

Iturrino, G. J., N. I Christensen, S. Kirby, and M. H. Salisbury (1991), Seismic velocities and elastic properties of oceanic gabbroic rocks from hole 735B, in *Proceedings of the Ocean Drilling Program, Scientific Results,* vol. 118, edited by R. P. von Herzen, et al., pp. 227–244, College Station, Tex.

Ivandic, M., I. Grevemeyer, A. Berhorst, E. R. Flueh, and K. McIntosh (2008), Impact of bending related faulting on the seismic properties of the incoming oceanic plate offshore of Nicaragua, *J. Geophys. Res.*, *113*, B05410, doi:10.1029/2007JB005291.

Iyer, K., L. H. Rüpke, J. Phipps Morgan, and I. Grevemeyer (2012), Controls of faulting and reaction kinetics on serpentinization and double Benioff zones, *Geochem. Geophys. Geosyst.*, *13*, Q09010, doi:10.1029/2012GC004304.

Kahle, R. L. (2007), A seismic investigation of the 21.5° propagating segment on the Mid-Atlantic Ridge, PhD thesis, pp. 176, St. John's Coll., Univ. of Cambridge, Cambridge.

Kanamori, H. (1983), Magnitude scale and quantification of earthquakes, *Tectonophysics*, *93*, 185–199.

King, G. C. P., R. S. Stein, and J. Lin (1994), Static stress changes and the triggering of earthquakes, *Bull. Seismol. Soc. Am.*, *84*, 935–953.

Kong, L. S. L., S. C. Solomon, and G. M. Purdy (1992), Microearthquake characteristics of a Mid-Ocean Ridge along-axis high, *J. Geophys. Res.*, *97*, 1659–1685, doi:10.1029/91JB02566.

Lefeldt, M., I. Grevemeyer, J. Gossler, and J. Bialas (2009), Intraplate seismicity and related mantle hydration at the Nicaraguan trench outer rise, *Geophys. J. Int.*, *178*, 742–752, doi:10.1111/j.1365-246X.2009.04167.x.

Lienert, B. R., and J. Havskov (1995), Hypocenter 3.2: A computer program for locating earthquakes locally, regionally and globally, *Seismol. Res. Lett.*, *66*, 26–36.

Lienert, B. R., E. Berg, and L. N. Frazer (1986), Hypocenter: An earthquake location method using centered, scaled, and adaptively least squares, *Bull. Seismol. Soc. Am.*, *76*, 771–783.

Martin, B., and W. S. Fyfe (1970), Some experimental and theoretical observations on the kinetics of hydration reactions with particular reference to serpentinization, *Chem. Geol.*, *6*, 185–202, doi:10.1016/0009–2541(70)90018-5.

Miller, D. J., and N. I. Christensen (1997), Seismic velocities of lower crustal and upper mantle rocks from the slow-spreading Mid-Atlantic Ridge, south of the Kane Transform Zone (MARK), in *Proceedings of the Ocean Drilling Program, Scientific Results*, vol. 153, edited by J. A. Karson, et al., pp. 437–454, College Station, Tex.

Minshull, T. A., N. J. Bruguier, and J. M. Brozena (2003), Seismic structure of the Mid-Atlantic Ridge, 8–9°S, *J. Geophys. Res.*, *108*(B11), 2513, doi:10.1029/2002JB002360.

Minshull, T. A., M. R. Muller, and R. S. White (2006), Crustal structure of the Southwest Indian Ridge at 66°E: Seismic constraints, *Geophys. J. Int.*, *166*, 135–147, doi:10.1111/j.1365-246X.2006.03001.x.

Mitchell, N. C. (1991), Distributed extension at the Indian Ocean Triple Junction, *J. Geophys. Res.*, *96*, 8019–8043.

Nettles, M., and G. Ekström (1998), Faulting mechanism of anomalous earthquakes near Bárdarbunga Volcano, Iceland, *J. Geophys. Res.*, *103*(B8), 17,973–17,983, doi:10.1029/98JB01392.

Petersen, S., et al. (2009), The geological setting of the ultramafic-hosted Logatchev hydrothermal field (14°45′N, MAR) and its influence on massive sulphide formation, *Lithos*, *112*(1–2), 40–56, doi:10.1016/j.lithos.2009.02.008.

Reston, T. J., and C. R. Ranero (2011), The 3-D geometry of detachment faulting at mid-ocean ridges, *Geochem. Geophys. Geosyst.*, *12*, Q0AG05, doi:10.1029/2011GC003666.

Reston, T. J., W. Weinrebe, I. Grevemeyer, E. R. Flueh, N. C. Mitchell, L. Kristein, C. Kopp, H. Kopp, and Gershwin Scientific Party (2002), A rifted inside corner massif on the Mid-Atlantic Ridge at 5°S, *Earth Planet. Sci. Lett.*, *200*, 255–269.

Richter, C. F. (1935), An instrumental earthquake magnitude scale, *Bull. Seismol. Soc. Am.*, *25*, 1–32.

Rubin, A. M., and D. D. Pollard (1988), Dike-induced faulting in rift zones of Iceland and Afar, *Geology*, *16*, 413–417, doi:10.1130/0091-7613(1988)016<0413:DIFIRZ>2.3.CO;2.

Salisbury, M. H., et al., (1988), Old oceanic crust: Synthesis of logging, laboratory, and seismic data from Leg 102, in *Proceedings of the Ocean Drilling Program, Scientific Results*, vol. 102, edited by M. H. Salisbury, et al., pp. 155–180, College Station, Tex.

Schmidt, K., A. Koschinsky, D. Garbe-Schönberg, L. M. De Carvalho, and R. Seifert (2007), Geochemistry of hydrothermal fluids from the ultramafic-hosted Logatchev hydrothermal field, 15°N on the Mid-Atlantic Ridge: Temporal and spatial investigation, *Chem. Geol.*, *242*, 1–21, doi:10.1016/j.chemgeo.2007.01.023.

Shipboard Scientific Party (2004), Site 1270, in *Proc. Ocean Drill. Program, Initial Rep. 209*, edited by P. B. Kelemen, et al., pp. 1–188, Ocean Drilling Program, College Station, Tex., doi:10.2973/odp.proc.ir.209.105.2004.

Simao, N., J. Escartin, J. Goslin, J. Haxel, M. Cannat, and R. Dziak (2010), Regional seismicity of the Mid-Atlantic Ridge: Observations from autonomous hydrophone arrays, *Geophys. J. Int.*, *183*, 1559–1578, doi:10.1111/j.1365-246X.2010.04815.x.

Smith, D. K., J. Escartin, M. Cannat, M. Tolstoy, C. G. Fox, D. R. Bohnenstiehl, and S. Bazin (2003), Spatial and temporal distribution of seismicity along the northern Mid-Atlantic Ridge (15°–35°N), *J. Geophys. Res.*, *108*(B3), 2167, doi:10.1029/2002JB001964.

Smith, D. K., J. R. Cann, and J. Escartín (2006), Widespread active detachment faulting and core complex formation near 13°N on the Mid-Atlantic Ridge, *Nature*, *442*, 440–443, doi:10.1038/nature04950.

Snoke, J. A., J. W. Munsey, A. G. Teague, and G. A. Bollinger (1984), A program for focal mechanism determination by combined use of polarity and SV-P amplitude ratio data, *Earthquake Notes*, *55*(3), 15.

Sykes, L. R. (1967), Mechanism of earthquakes and nature of faulting on the mid-ocean ridge, *J. Geophys. Res.*, *72*, 2131–2153.

Tilmann, F., E. Flueh, L. Planert, T. Reston, and W. Weinrebe (2004), Microearthquake seismicity of the Mid-Atlantic Ridge at 5°S: A view of tectonic extension, *J. Geophys. Res.*, *109*, B06102, doi:10.1029/2003JB00282.

Tivey, M. A., and B. E. Tucholke (1998), Magnetization of oceanic crust from 0 to 29 Ma formed at the Mid-Atlantic Ridge 25°30′ to 27°10′N, *J. Geophys. Res.*, *103*, 17,807–17,826.

Toomey, D. R., S. C. Solomon, and G. M. Purdy (1988), Microearthquakes beneath median valley of Mid-Atlantic Ridge near 23°N: Tomography and tectonics, *J. Geophys. Res.*, *93*, 9093–9112, doi:10.1029/JB093iB08p09093.

Tucholke, B. E., J. Lin, and M. C. Kleinrock (1998), Mega-mullions and mullion structure defining oceanic metamorphic core complexes on the mid-Atlantic ridge, *J. Geophys. Res.*, *103*, 9857–9866, doi:10.1029/98JB00167.

Vine, F. J., and D. H. Matthews (1963), Magnetic anomalies over oceanic ridges, *Nature*, *199*, 947–949.

Vogt, P. R. (1986), Magnetic anomalies and crustal magnetization, in *The Western Atlantic Region, The Geology of North America*, edited by P. R. Vogt and B. E. Tucholke, pp. 229–256, Geol. Surv. of Am., Boulder, Colo.

Wessel, P., and W. H. F. Smith (1995), New version of the generic mapping tools released, *Eos Trans. AGU*, *76*, 329.

White, R. S., J. Drew, H. R. Martens, J. Key, H. Soosalu, and S. S. Jakobsdóttir (2011), Dynamics of dyke intrusion in the mid-crust of Iceland, *Earth Planet. Sci. Lett.*, *304*, 300–312.

Wilcock, W. S. D., S. D. Archer, and G. M. Purdy (2002), Microearthquakes on the Endeavour segment of the Juan de Fuca Ridge, *J. Geophys. Res.*, *107*(B12), 2336, doi:2310.1029/2001JB000505.

Wilcock, W. S. D., E. E. E. Hooft, D. R. Toomey, P. R. McGill, A. H. Barclay, D. S. Stakes, and T. M. Ramirez (2009), The tole of magma injection in localizing black-smocker activity, *Nat. Geosci.*, *2*, 509–513.

Williams, C. M., R. A. Stephen, and D. K. Smith (2006), Hydroacoustically recorded seismicity at the intersection of the Atlantis (30°N) and Kane (23°40′N) Transform faults with the mid-Atlantic ridge, *Geochem. Geophys. Geosyst.*, *7*, Q06015, doi:10.1029/2005GC001127.

Wolfe, C. J., G. M. Purdy, D. R. Toomey, and S. C. Solomon (1995), Microearthquake characteristics and crustal velocity structure at 29°N on the Mid-Atlantic Ridge: The architecture of a slow spreading segment, *J. Geophys. Res.*, *100*, 24,449–24,472, doi:10.1029/95JB02399.

Wyss, M., K. Shimazaka, and S. Wiemer (1997), Mapping active magma chambers by b values beneath the off-Ito volcano, *J. Geophys. Res.*, *10*, 20,413–20,422.